Key Points:

- We implement a spheroidal model for dust shape along with the porosity to examine dust morphology effects in a chemical transport model
- Nonspherical dust particles with pores increase surface area available for reactive uptake
- Spheroidal rather than spherical dust treatment reduces the effects of aerosols on UV-Vis NO$_2$ retrievals by factors of 2.0–2.5

Correspondence to:

I. Singh,
inderjeet.singh@wustl.edu

Author Contributions:

Conceptualization: Inderjeet Singh, Randall V. Martin, Deepangsu Chatterjee, Chi Li, Christopher Oxford
Formal analysis: Inderjeet Singh
Funding acquisition: Randall V. Martin
Methodology: Inderjeet Singh
Software: Liam Bindle, Xiaoguang Xu, Jun Wang
Supervision: Randall V. Martin
Validation: Randall V. Martin
Visualization: Inderjeet Singh
Writing – original draft: Inderjeet Singh
Writing – review & editing: Randall V. Martin

Effect of Dust Morphology on Aerosol Optics in the GEOS-Chem Chemical Transport Model, on UV-Vis Trace Gas Retrievals, and on Surface Area Available for Reactive Uptake

Inderjeet Singh[1] , **Randall V. Martin[1]** , **Liam Bindle[1], Deepangsu Chatterjee[1], Chi Li[1]** , **Christopher Oxford[1], Xiaoguang Xu[2]** , **and Jun Wang[3]**

[1]Department of Energy, Environment and Chemical Engineering, Washington University in St. Louis, St. Louis, MO, USA, [2]Goddard Earth Sciences Technology and Research II, University of Maryland Baltimore County, Baltimore, MD, USA, [3]Department of Chemical and Biological Engineering, Iowa Technology Institute, Center for Global and Regional Environmental Research, University of Iowa, Iowa City, IA, USA

Abstract Many chemical transport models treat mineral dust as spherical. Solar backscatter retrievals of trace gases (e.g., OMI and TROPOMI) implicitly treat mineral dust as spherical. The impact of the morphology of mineral dust particles is studied to assess its implications for global chemical transport model (GEOS-Chem) simulations and solar backscatter trace gas retrievals at ultraviolet and visible (UV-Vis) wavelengths. We investigate how the morphology of mineral dust particles affects the simulated dust aerosol optical depth; surface area, reaction, and diffusion parameters for heterogeneous chemistry; phase function, and scattering weights for air mass factor (AMF) calculations used in solar backscatter retrievals. We use a mixture of various aspect ratios of spheroids to model the dust optical properties and a combination of shape and porosity to model the surface area, reaction, and diffusion parameters. We find that assuming spherical particles can introduce size-dependent and wavelength-dependent errors of up to 14% in simulated dust extinction efficiency with corresponding error in simulated dust optical depth typically within 5%. We find that use of spheroids rather than spheres increases forward scattered radiance and decreases backward scattering that in turn decrease the sensitivity of solar backscatter retrievals of NO$_2$ to aerosols by factors of 2.0–2.5. We develop and apply a theoretical framework based on porosity and surface fractal dimension with corresponding increase in the reactive uptake coefficient driven by increased surface area and species reactivity. Differences are large enough to warrant consideration of dust non-sphericity for chemical transport models and UV-Vis trace gas retrievals.

Plain Language Summary Mineral dust is often treated as spherical in chemical transport and trace gas retrieval models. In this study, we investigate how dust shape affects gas-particle and radiation-particle interactions. We examine the impact of dust shape on optical properties and trace gas retrievals at ultraviolet and visible wavelengths. We find that treating dust as nonspherical in trace gas retrievals of nitrogen dioxide decreases the retrieval sensitivity to dust. We also examine the impact of dust shape on heterogeneous chemistry by developing and applying a theoretical model. We find that dust pores change particle surface area significantly and subsequently, reaction and diffusion parameters. Overall, this study signifies the importance of accounting for nonsphericity in chemical transport and trace gas retrieval models.

1. Introduction

Mineral dust is the most abundant aerosol by mass in the atmosphere and one of the key constituents of atmospheric aerosols (Formenti et al., 2003; Kok et al., 2017, 2018). These particles have complex morphology (shape and surface characteristics) which affects retrievals (Mishchenko et al., 1997; Wang et al., 2003). Dust morphology also affects the heterogeneous chemistry of trace gases in the atmosphere by providing surfaces for trace gas adsorption and reaction (Jacob, 2000). Many significant advances have been made for accurate representation of the shape of dust particles in aerosol remote sensing applications (Dubovik et al., 2002; Kahn et al., 1997; Kalashnikova et al., 2005; Liu et al., 1999). However, representation of dust non-sphericity in chemical transport models (CTMs) is rare. CTMs require dust representation to interpret satellite observations of aerosol optical depth to assess aerosol radiative effects (Ginoux et al., 2001, 2004), for air quality assessment (van Donkelaar et al., 2006), and to interpret field observations of trace gases and aerosols which are affected by

heterogeneous reactions with mineral dust (Fairlie et al., 2010; Zhai et al., 2023). Atmospheric optical properties from CTMs are relied upon to calculate scattering weights and averaging kernels for trace gas retrievals from solar backscatter measurement in ultraviolet and visible (UV-Vis) wavelengths (Eskes & Boersma, 2003; Palmer et al., 2001) including accounting for aerosol effects (Cooper et al., 2019; J.-T. Lin et al., 2015). In this paper, we examine how the shape and surface characteristics of dust particles affect the modeling of aerosol optical depth; surface area for heterogeneous chemistry, reaction and diffusion parameters; and UV-Vis trace gas retrievals.

Dust particles are generally nonspherical without a typical shape as apparent from dust scanning electron microscopy images (Gao & Anderson, 2001; Okada et al., 2001; Reid et al., 2003). The simplest mathematical geometry used to model dust shape is a sphere which can be described by a single degree of freedom (radius). However, multiple studies have shown that spheres do not produce accurate results for dust optical properties and therefore, radiative transfer calculations (Kahnert & Kylling, 2004; Kalashnikova & Sokolik, 2002, 2004; Mishchenko et al., 1997). The most widely applied shape to model nonsphericity of dust particles is the spheroidal geometry; mathematically described by two degrees of freedom (aspect ratio and radius). Mishchenko et al. (1997) examined the benefits of using spheroids to model the phase function of nonspherical dust particles and found that a mixture of randomly oriented, polydisperse, and homogeneous spheroids with different axis ratios could reproduce measured phase functions. Although subsequent studies assumed more complex and realistic shapes to simulate the optical properties (Bi et al., 2010; Kalashnikova & Sokolik, 2002; P. Yang et al., 2000), such simulations are only applicable for a small size range of dust aerosols. Nonetheless, the exact particle shape used to reproduce the scattering properties is unimportant (Bohren & Singham, 1991; Mishchenko et al., 1997) because bulk scattering results are averaged over different shapes and orientations of individual particles.

The reaction uptake coefficient, which is a fundamental parameter to represent heterogeneous chemistry in chemical transport models (Dentener et al., 1996; Jacob, 2000) depends on the surface characteristics. Huang et al. (2015) found that the porosity of dust particles affects reactive uptake coefficients significantly. Porosity both increases the dust surface area while decreasing the mass transfer rate (diffusion rate) of the gaseous species to the internal surface of the mineral dust, thus limiting the internal surface area available for reaction. We attempt to model these changes analytically to demonstrate the effects of surface heterogeneity on dust chemistry.

Dust shape may have implications for trace gas (e.g., NO_2, SO_2, HCHO) retrievals from solar backscattered measurements in the UV-Vis part of electromagnetic spectrum using satellite instruments such as OMI (Levelt et al., 2006), TROPOMI (Veefkind et al., 2012), GEMS (Kim et al., 2020) and TEMPO (Zoogman et al., 2017). The retrieval algorithms use an air mass factor (AMF) that includes a radiative transfer calculation of the vertically resolved sensitivity to the trace gas of interest, to convert line of sight slant column density to vertical column density (Eskes & Boersma, 2003; Palmer et al., 2001). Aerosol effects on AMF calculations can be summarized into four categories: enhancement effect (increase AMF), reflectance effect (increase AMF), shielding effect (decreases AMF) and absorption effect (decreases AMF) (Cooper et al., 2019). Operational retrievals such as DOMINO (Boersma et al., 2011) and $OMNO_2$ (Bucsela et al., 2006) often implicitly treat aerosols as spheres using Mie scattering computations. Research algorithms have explicitly treated aerosols effects using specific aerosol types, but included mineral dust as spherical (Jung et al., 2019; J.-T. Lin et al., 2014, 2015; Martin et al., 2003). The effect of mineral dust shape warrants investigation due to its effects on the light path.

The overall objectives of this study are to: (a) Study the impacts of applying the spheroidal model for dust shape on calculations of aerosol optical depth in a widely used chemical transport model (GEOS-Chem); (b) Study the implications of applying a spheroidal model for dust shape on UV-Vis trace gas retrievals, and (c) Investigate the impacts of both shape and surface irregularities on heterogeneous chemistry by studying the change in the surface area, reaction and diffusion parameters. We adopt the following strategy to develop an approach that links the impact of the morphology of mineral dust particles to their optical properties, aerosol optical depth and AMF; and to surface area, and reaction and diffusion parameters. First, we calculate optical properties of spherical and spheroidal particles and their relative difference using *T*-matrix and Mie theory (Mishchenko et al., 2002). A new lookup table is made for the optical properties of spheroidal dust and applied in a global chemical transport model (GEOS-Chem) to estimate the change in aerosol optical depth. Then, we calculate the change in the scattering weights using the Unified Linearized Vector Radiative Transfer Model (UNL-VRTM) (Xu & Wang, 2019) which uses the VLIDORT (Linearized vector discrete ordinate radiative transfer) algorithm (Spurr, 2006) to solve

radiative transfer equations. We ignore the effects of surface irregularities on the optical properties as these effects are averaged out when considering polydispersity, random orientations and different aspect ratios (Li et al., 2004; Zubko et al., 2007). Finally, we simulate the change in the surface area of spherical and spheroidal dust particles using GEOS-Chem, and study of the impacts of surface irregularities on surface area, and reaction and diffusion parameters using a theoretical framework developed here.

2. Dust in GEOS-Chem

We use the GEOS-Chem model version 12.7.2 to simulate the global distribution of dust parameters affecting AOD and surface area. GEOS-Chem is a three-dimensional chemical transport model first described by Bey et al. (2001) that is driven by assimilated meteorological data from the Goddard Earth Observing System (GEOS). We use GEOS-FP meteorological fields for the year 2016 with a horizontal resolution of 4° (latitude) × 5° (longitude) and 72 vertical layers between the surface and 0.01 hPa. The spin-up time for these simulations is 1 month. The standard dust mobilization scheme in GEOS-Chem is the dust entrainment and deposition (DEAD) scheme supplemented by a source function from Ginoux et al. (2001) as described by Fairlie et al. (2007) and updated by Meng et al. (2021).

The total mass of dust in GEOS-Chem is divided into four independently transported size bins with size ranges 0.1–1, 1–1.8, 1.8–3 and 3–6 μm with effective radii (r_{eff}) of 0.75, 1.5, 2.5, and 4 μm respectively following Tegen and Lacis (1996) and Ginoux et al. (2001). The mass fraction emitted in each bin is 0.077, 0.192, 0.349 and 0.382. The smallest bin is further subdivided into 4 size bins with effective radii 0.15, 0.25, 0.4, 0.8 μm to calculate optical properties, heterogeneous chemistry and photochemistry; each bin has the mass fraction of 0.007, 0.033, 0.249 and 0.711 as described by Zhang et al. (2013). The current look-up table which contains optical properties of dust particles is based on Mie theory using a standard gamma size distribution function following Tegen and Lacis (1996) as originally implemented in GEOS-Chem by Martin et al. (2003). In the following section, we update this look-up table for nonspherical particles with a log-normal size distribution.

3. Optical Tables Needed for Chemical Transport Models Depend on Dust Shape

We use Mie theory and the T-matrix method (Mishchenko et al., 2002) to calculate the optical properties of spherical and spheroidal dust, respectively at 12 wavelengths (λ) between 300 and 1,020 nm. The T-matrix method also known as the Extended Boundary Condition Method is based on an integral formulation of the scattering problem. The coefficients of the vector spherical harmonics used to expand the incident and scattered field can be related using a transition matrix (or T-matrix) because of the linearity of the Maxwell equations and boundary conditions. A fundamental feature of the T-matrix approach is that T-matrix elements only depend on the physical and geometric characteristics of the scattering particles (shape, size parameter, refractive index and on the orientation of the particle with respect to the reference frame) and are independent of the incident and scattering fields (propagation direction and polarization state). Although, the inability of the T-matrix code to calculate the optical properties for larger size parameters ($x_{eff} = \frac{2\pi r_{eff}}{\lambda} > 35$) with extreme aspect ratios (<0.45 for oblate spheroids) limits our calculations to fewer aspect ratios for large size parameters, we perform calculations for the aspect ratios at which the solution does converge as listed in Table A1 of Appendix A along with the size parameter range.

The size distribution for dust particles is treated as log-normal and expressed as

$$n(r) = \frac{C}{r} \exp\left[\frac{-(\ln r - \ln r_g)^2}{2 \ln^2 \sigma_g}\right] \tag{1}$$

where r is radius, r_g is the geometric mean radius, σ_g is the geometric standard deviation, and C is a constant that can be evaluated using the normalization condition (2).

$$\int_{r_{min}}^{r_{max}} n(r)\, dr = 1 \tag{2}$$

In Equation 1, r is the radius for spherical particles and equivalent volume radius for spheroidal particles. The corresponding effective radii r_{eff} (Hansen & Travis, 1974) are expressed for the 6 bins as

$$r_{\text{eff}} = \frac{1}{<G>} \int_{r_{\min}}^{r_{\max}} \pi r^3 \, n(r) \, dr \tag{3}$$

where

$$<G> = \int_{r_{\min}}^{r_{\max}} \pi r^2 \, n(r) \, dr \tag{4}$$

$<G>$ is the geometric projected area. Here we develop a method to compute the value of $<G>$ for spheroidal particles. The projected area for a spheroid having a random orientation is given by Bi and Yang (2014).

$$A_{\text{prolate}} = \frac{\pi a^2}{2}\left[1 + \frac{\gamma}{e}\sin^{-1}(e)\right], e = \sqrt{1 - \gamma^{-2}} \ \text{ if } \ a < c \tag{5}$$

$$A_{\text{oblate}} = \frac{\pi a^2}{2}\left[1 + \frac{1 - e^2}{e}\tanh^{-1}(e)\right], e = \sqrt{1 - \gamma^2} \ \text{ if } \ a > c \tag{6}$$

where e is eccentricity; $\gamma = \frac{c}{a}$ is aspect ratio; a and c are semi-axes of the spheroid. If $a = c$, the spheroid will be transformed into a sphere as eccentricity e is zero. A represents projected area averaged over random orientations.

To calculate the average projected area per particle for a given size range and size distribution, we replace πr^2 in Equation 4 with the projected area of a spheroid A

$$<G>_{\text{spheroid}} = \int_{r_{\min}}^{r_{\max}} A \, n(r) \, dr \tag{7}$$

We have treated r as a volume equivalent radius in size distribution function for spheroidal particles which can be derived as

$$\frac{4}{3}\pi r^3 = \frac{4}{3}\pi c a^2; \tag{8}$$

thus,

$$r = a \, \gamma^{\frac{1}{3}} \tag{9}$$

Using the above expressions, we derive the following relation between the geometric projected area of a sphere and the geometric projected area of an equal volume spheroid for

$$\frac{<G>_{\text{prolate}}}{<G>_{\text{sphere}}} = \frac{1}{2\gamma^{\frac{2}{3}}}\left[1 + \frac{\gamma}{e}\sin^{-1}(e)\right] = f(\gamma) \tag{10}$$

$$\frac{<G>_{\text{oblate}}}{<G>_{\text{sphere}}} = \frac{1}{2\gamma^{\frac{2}{3}}}\left[1 + \frac{1 - e^2}{e}\tanh^{-1}(e)\right] = f(\gamma) \tag{11}$$

Equations 10 and 11 imply that the ratio of projected areas of spheroidal to spherical particles is a function of aspect ratio only. The term on the right side of the equation is the sphericity factor, which is the same for the ratio of the surface area of spheroidal and spherical shape particles for equal volumes (Ginoux, 2003).

We calculate the projected area of spheroidal particles from Equations 10 and 11. We used an equiprobable mixture of prolate and oblate spheroids with 26 aspect ratios ranging from 1.2 to 2.4 with a step size of 0.1 with a median aspect ratio of 1.8 following the approach of Mishchenko et al. (1997). The chosen aspect ratio is in

reasonable agreement with laboratory measurements of particle shape conducted by Nakajima et al. (1989) and Okada et al. (1987) which found that the mode aspect ratio of soil particles and desert dust aerosol was about 1.7. We calculate the sphericity factor and projected areas of the spheroids for these 26 aspect ratios. We use these projected areas to calculate the mean extinction efficiency Q_{ext} of the spheroidal dust particles and in turn aerosol optical depth (τ) as a function of GEOS-Chem mass loading (M)

$$\tau = \frac{3}{4} \frac{M \cdot Q_{ext}}{P \cdot r_{eff}} \tag{12}$$

where P is particle mass density which is treated as 2,500 kg/m^2 for submicron particles and 2,650 kg/m^2 for particles greater than 1 μm following Ginoux et al. (2001).

Figure 1 shows for seven size bins, the extinction efficiency versus size parameter for spherical and spheroidal particles and their difference. The extinction efficiency for spheroids is similar to that for spheres, with a steep increase in extinction efficiency for small size parameter (<3), a resonance peak when the particle radii approach the wavelength of radiance, and an asymptotic approach to the value of 2 for large size parameters (>10). However, differences between spheroidal and spherical particles are apparent for size parameters less than 10. The extinction efficiency for spheroidal particles exhibits a broader and shallower resonance peak than for spherical particles, reflecting the broader distribution of aspect ratios for spheroidal particles. In addition, spherical particles exhibit a damped oscillatory pattern in the extinction efficiency, a typical signature for particles with small effective variance (Appendix A). This pattern disappears for spheroidal particle over a distribution of aspect ratios. Thus, the difference between extinction efficiencies of spheroidal and spherical particles exhibits oscillatory behavior.

Figure 2 shows the corresponding relative differences of extinction efficiencies versus wavelength for the 7 size bins. The relative differences approach 14% at wavelengths and particle sizes similar to each other which occurs near the resonance peak in extinction efficiency. Most of the difference appears in submicron size bins, which comprise an important fraction of the total aerosol optical depth (Figure B1). We also explore the relative difference of absorption efficiencies versus wavelength using single scattering albedo (Figure A1). Positive relative differences appear in the submicron size bins with maximum of 11% and negative differences appear at super micron sizes with maximum amplitude of −6%. Non-spherical particles tend to absorb more than spherical particles as size increases. We update the look-up table of dust optical properties in GEOS-Chem to represent spheroidal particles as given in Appendix C.

We simulate the aerosol optical depth using the updated look-up table in GEOS-Chem for the year 2017. We focus on τ at 550 nm for 0.15 μm radius and 800 nm for 0.8 μm radius which correspond to the largest differences in the extinction efficiency. We find that total global dust aerosol optical depth decreases by 1.65% at 550 nm and increases by 4.05% at 800 nm with larger differences for some sizes at specific wavelengths. The weaker sensitivity to particle morphology of total dust τ compared with τ at specific wavelengths reflects the contribution from multiple sizes with variable sensitivity to particle morphology at a specific wavelength. These findings are consistent with Mishchenko et al. (1997). Overall, the impact of the shape on simulated τ is typically within 5% (Figure B2). We also compare GEOS-Chem simulated total AOD at 550 nm with AERONET (Figure B3). The spheroid model does not introduce significant changes in the comparison as AOD (r^2 remains unchanged) is more strongly influenced by other factors. Nonetheless, wavelength-specific differences could have implications for comparisons of simulated τ with observations at specific wavelengths such as examined in the next section.

4. Dust Shape, Intensity and Scattering Weights

We use the Unified Linearized Vector Radiative Transfer Model (UNL-VRTM) (Xu & Wang, 2019) to study the impact of particle morphology on scattered radiance and on the scattering weights for AMF calculations. UNL-VRTM uses the VLIDORT algorithm (Spurr, 2006) as the radiative transfer equation solver. The required inputs for the model consist of atmospheric extinction, single scattering albedo, moments of the phase function, solar zenith angle, solar azimuth angle, and viewing azimuth angle. We use a Lambertian surface with surface reflectance 0.15 at 440 nm for Riyadh, Saudi Arabia (latitude = 24.71°N, longitude = 46.67°E) provided by TROPOMI surface LER (Lambertian-equivalent reflectivity) and DLER (Directional dependent Lambertian reflectivity) database (https://www.temis.nl/surface/albedo/tropomi_ler.php, last accessed 1 December 2022).
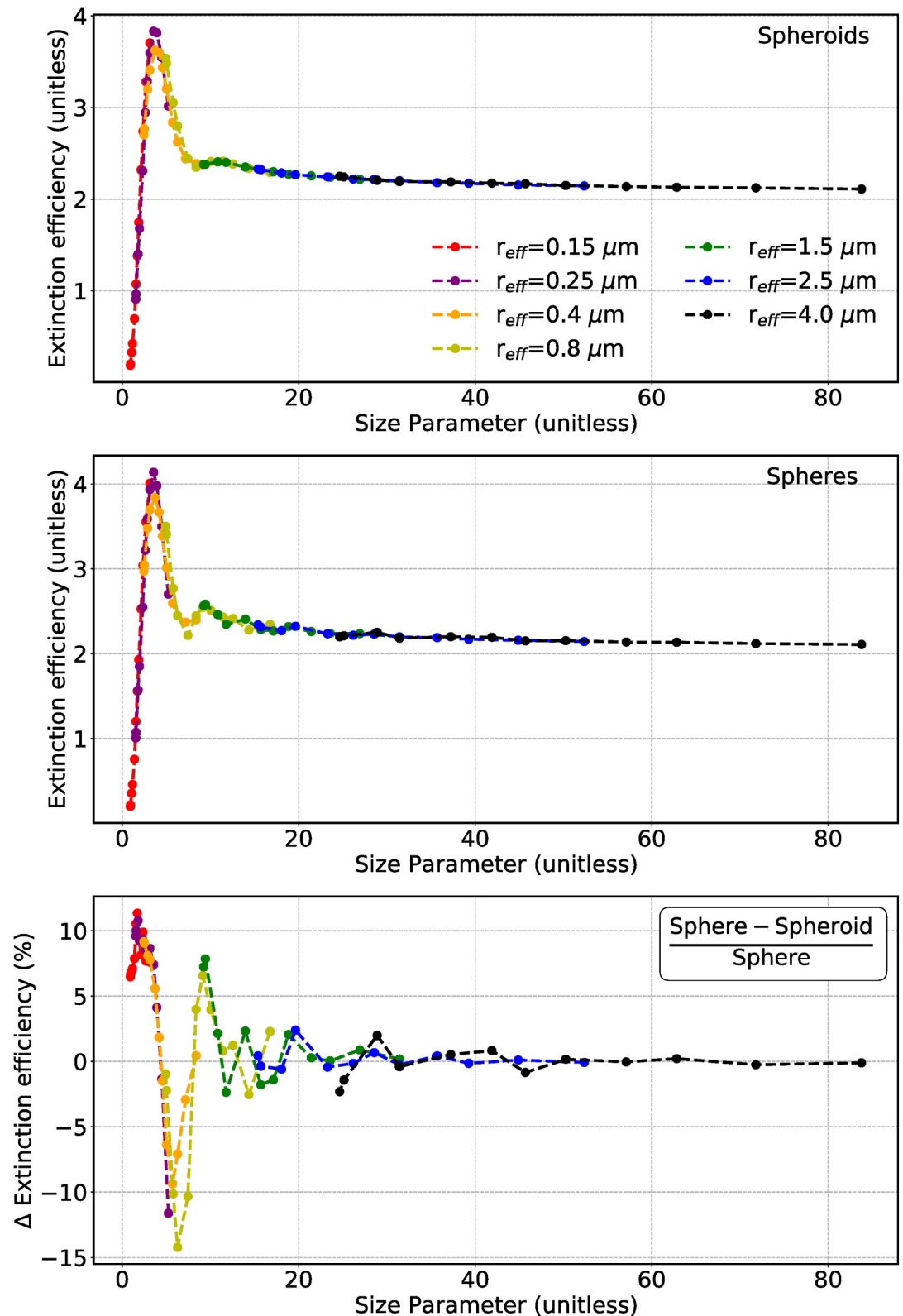
Figure 1. Extinction efficiency (Q_{ext}) versus effective size parameter (x_{eff}) for spheroids (top), extinction efficiency versus size parameter for spheres (middle), change in extinction efficiency versus size parameter (bottom). Each colored line represents an effective radius (r_{eff}) for the given size range and bold points denote the size parameter ($x_{eff} = 2\pi r_{eff}/\lambda$). The spectral refractive indices are tabled in Appendix C following Sinyuk et al. (2003).
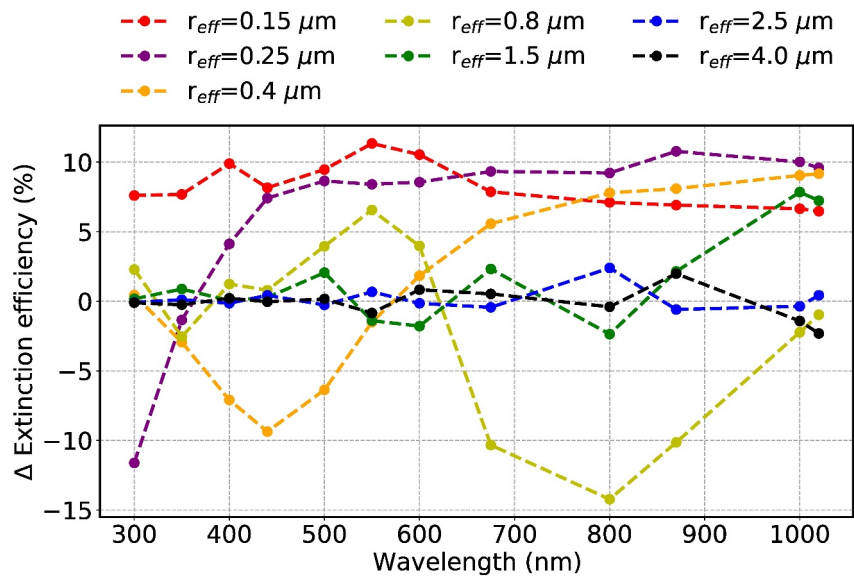
Figure 2. Relative difference in extinction efficiency $\left(\frac{(Q_{\text{sphere}} - Q_{\text{spheroid}}) * 100}{Q_{\text{sphere}}}\right)$ versus wavelength.

We assume a Rayleigh atmosphere with dust uniformly distributed up to 4 km altitude with optical thickness of 0.3. The input irradiance is 2.03×10^3 mW/m^2/nm.

We use the following (Equation 13 for downwelling and Equation 14 for upwelling) to calculate the scattering angle Θ from the given set of the sensor zenith angles (θ), relative azimuth angles ($\Delta\phi$) and solar zenith angle (θ_0) (Liou, 2002).

$$\cos(\Theta) = \cos\theta \times \cos\theta_0 + \sin\theta \times \sin\theta_0 \times \cos(\Delta\phi) \tag{13}$$

$$\cos(\pi - \Theta) = \cos\theta \times \cos\theta_0 + \sin\theta \times \sin\theta_0 \times \cos(\Delta\phi) \tag{14}$$

Solar and viewing zenith angles vary from −90° to 90° and solar and viewing azimuth angles are defined clockwise with range [0, 360].

To calculate the specific intensity change, we first examine the phase function of spherical as well as spheroidal dust particles. Numerous studies have shown the impact of the shape of particles on the phase function (Dubovik et al., 2006; Kalashnikova & Sokolik, 2002, 2004; Mishchenko et al., 2002). Figure 3 shows the phase function of spherical dust particles (blue curve) and averaged phase function of spheroidal dust particles (red curve) at
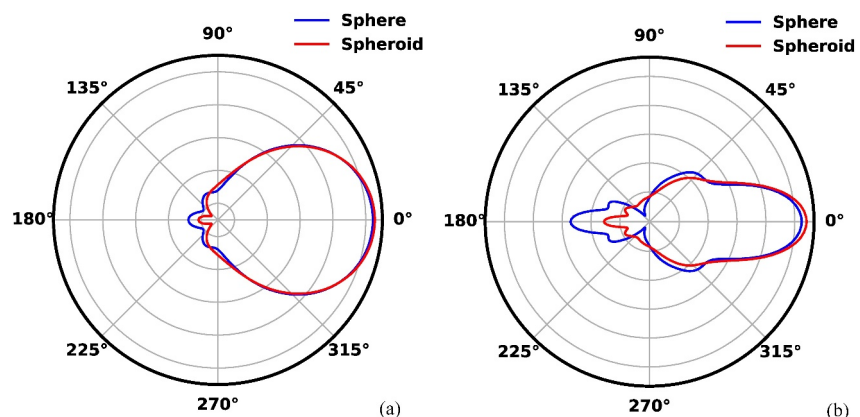
Figure 3. Phase function of spheres (blue) and ensemble average phase function of spheroidal dust particles (red) for (a) $r_{\text{eff}} = 0.15$ μm at 350 nm (b) $r_{\text{eff}} = 0.4$ μm at 440 nm. Gray circles indicate the logarithm of phase function (in sr^{-1}).

Table 1
Relative Differences in the Radiance (L) of Spherical and Spheroid Shape Dust Particles Calculated at Various Scattering Angles

Scattering angles	Viewing zenith angles	Relative azimuth angles	Radiance (sphere)	Radiance (spheroid)	Relative difference (%)
0.00	30.00	0.00	428.25	503.52	17.58
14.87	15.00	0.00	177.36	192.48	8.53
18.45	15.00	30.00	127.39	137.36	7.83
39.48	15.00	120.00	51.94	50.19	−3.37
51.31	30.00	120.00	50.27	45.72	−9.05
120.00	30.00	360.00	56.53	57.82	2.28
130.50	60.00	240.00	72.18	73.88	2.36
150.00	60.00	180.00	84.90	81.06	−4.52
165.12	30.00	210.00	71.30	65.89	−7.59
180.00	30.00	180.00	90.31	71.23	−21.13

Note. All angles are in deg. and units of radiance are $mWm^{-2}sr^{-1} nm^{-1}$. The relative difference is calculated as $\left(\frac{(L_{spheroid} - L_{sphere}) * 100}{L_{sphere}}\right)$. The first five rows represent the downwelling diffuse spectral radiance at the bottom of the atmosphere and the last five rows show the upwelling diffuse spectral radiance measured at the top of the atmosphere.

wavelength 350 and 440 nm for r_{eff} 0.15 and 0.4 μm, respectively. These wavelengths are the center of HCHO (350 nm) and NO_2 (440 nm) fitting windows used to determine a slant column abundance. Using spheroids versus spheres for both forward scattering and backscattering for 0.15 μm at 350 nm ($x_{eff} = 2.69$) are within 3%. For 0.4 μm at 440 nm ($x_{eff} = 5.70$), spheroids induce a large (8%–21%) decrease in the backscattered radiance (around scattering angle 160–180°) and a small increase in both forward and side scattering (around scattering angle 120°–140°). Thus, the spherical model overestimates the backscattered radiance and underestimates the side and forward scattered radiance for 0.4 μm at 440 nm. The large sensitivity of backscattering of spheroidal compared to spherical particles is associated with dependence on the change in phase relation (Δp) of scattered wavelets from individual dipoles on the scattering angle ($\Delta p \propto (1 - \cos\Theta)$, thus high sensitivity at 180°) and distance between the dipoles (Bohren & Singham, 1991). As shape changes, the relative distance among the dipoles changes which affects backscattering.

To estimate the differences in the radiance due to the shape of the dust particles, we input single scattering albedo, the moments of the phase function, and cumulative dust optical depth of 0.3 of the spherical as well as spheroidal shape dust particles in the model. We focus on r_{eff} of 0.4 μm at 440 nm where there is a large and distinct difference in the phase function between spherical and spheroidal particles (Figure 3b). Table 1 shows results for a solar zenith angle of 30°.

The strong radiance at 0° scattering angle increases by 17.6% when changing from spheres to spheroids corresponding to the enhancement of forward scattering. At 180° scattering angle, there is an overestimation of 21.1% in the spectral radiance if spheres are used to represent the dust particles. Also apparent is the overestimation of scattered radiance at scattering angle between 20° and 90° and underestimation of side scattering at angles between 90° and 140°.

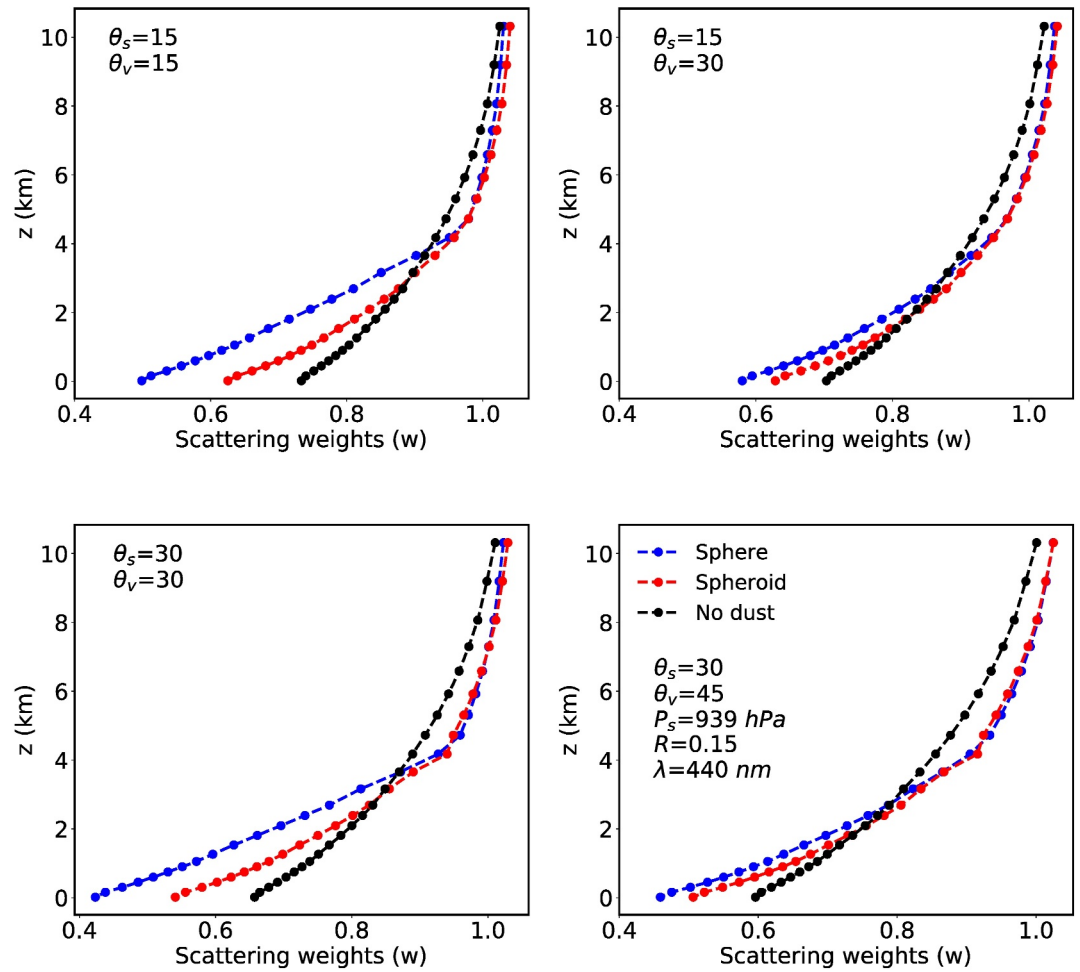We use UNL-VRTM to calculate the Jacobian of the intensity field which is an important parameter for the AMF calculation. The AMF is a function of scattering weights ($w(z)$) and shape factor ($S(z)$) (Palmer et al., 2001) as described by the following relation

$$AMF = AMF_G \int_0^{\infty} w(z) \, S(z) \, dz \tag{15}$$

where,

$$w(z) = -\frac{1}{AMF_G} \frac{\partial \ln I_B}{\partial \tau} \tag{16}$$

Figure 4. Scattering weights for the atmosphere below 10 km with dust ($\tau_{440} = 0.3$) uniformly distributed up to 4 km for 4 different viewing geometries. Scattering weights are calculated for wavelength (λ) of 440 nm, surface pressure (P_s) of 939 hPa and Lambertian surface reflectance (R) of 0.15.

$$S(z) = \frac{\alpha(z)\,n(z)}{\int_0^\infty \alpha(z)\,n(z)\,dz} \tag{17}$$

$$\mathrm{AMF}_G = \sec\theta_s + \sec\theta_v \tag{18}$$

AMF_G is the geometric AMF defined for a non-scattering atmosphere, a simple function of solar zenith angle θ_s and satellite viewing zenith angle θ_v. $\frac{\partial \ln I_B}{\partial \tau_l}$ is the local derivative of the backscattering intensity (I_B) with respect to layer optical depth τ_l and is equal to the $\frac{\mathrm{Jacobian}}{\tau_l I_B}$. $\alpha(z)$ and $n(z)$ are the absorption cross-section and number density of the absorbing air molecules, respectively. The Jacobian is defined as $\tau_l \frac{dI_B}{d\tau_l}$.

We calculate the scattering weights for r_{eff} of 0.4 μm at 440 nm ($x_{\mathrm{eff}} = 5.70$), a wavelength in the NO_2 absorption band (423–451 nm). Figure 4 shows scattering weights distribution with respect to height from surface for Riyadh, Saudi Arabia (Monthly mean P_s = 939 hPa) to 10 km for the month of July 2016 for different optical geometries with $\theta_s = 15°$, 30° and $\theta_v = 15°$, 30°, 45° for both spherical and spheroidal dust particles. The black line indicates the scattering weight profile calculated without dust (no dust). This signifies the importance of molecular scattering and how scattering weights deviate in the presence of aerosols (both spherical and non-spherical). Increasing θ_s and θ_v decreases scattering weights for clear sky implying the increased path length and attenuation due to scattering. The presence of a spherical dust layer (blue line) increases scattering weights near the top of the layer and above due
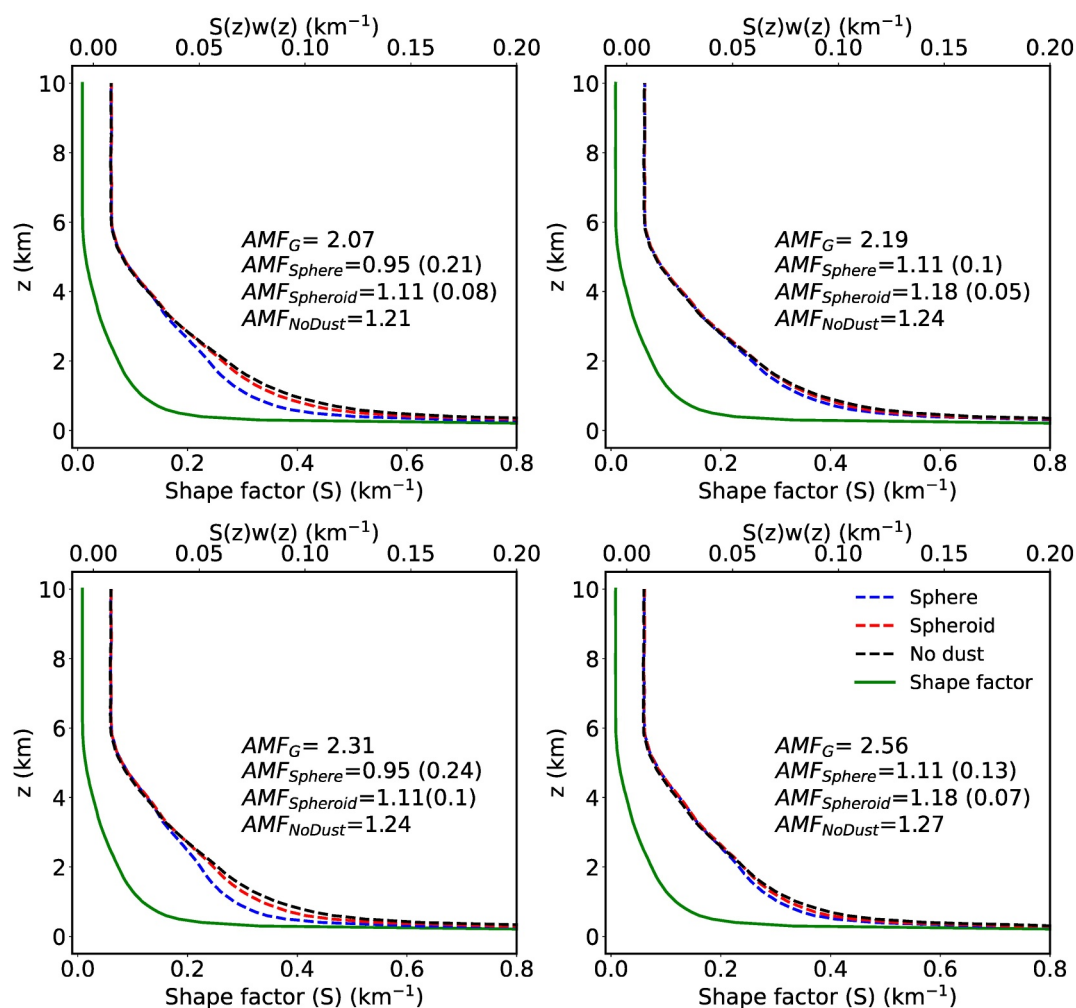
Figure 5. GEOS-Chem simulated monthly mean vertical shape factor (S) (solid green line) for NO_2 as a function of height z over Riyadh, Saudi Arabia. The blue, red and black lines represent the product $w(z)S(z)$, for spherical, spheroidal dust and clear sky (No dust), respectively. Values of air mass factor (AMF) calculated assuming spherical and spheroidal dust are also shown along with geometrical AMF (AMF_G) and clear sky AMF. Values in parentheses are the aerosol correction.

to increased backscattering by the aerosol below, while decreasing scattering weights below due to shielding (Cooper et al., 2019). Changing from spherical to spheroidal particles diminishes both effects by increasing forward scattering. The change in scattering weights also depends upon scattering angle (Θ). For equivalent θ_s and θ_v, the backscattering angle is 180° and spherical dust offers large backscattering which in turn, increases the shielding effect. Increasing both θ_v and θ_s increase the path length for the line of sight and hence, scattering weights decrease. However, for different θ_v and θ_s there is less backscattering relative to $\Theta = 180°$ hence, a smaller shielding effect and greater scattering weights. The average effect on scattering weights at the surface of spheroidal dust is a quarter to half that of spherical dust depending on geometry.

We use GEOS-Chem simulated monthly mean mixing ratio to generate an example shape factor over Riyadh. Figure 5 shows the NO_2 shape factor over Riyadh for July 2016 along with the product $w(z)S(z)$ for both spheroidal and spherical dust for four geometries. The product $w(z)S(z)$ provides a measure of NO_2 signal observed in a fitting spectral window. The $AMF_{Spheroid}$ increases with increasing θ_v and θ_s relative to AMF_{sphere}. We define an aerosol correction as the change in the AMF due to aerosol effects relative to the AMF without aerosols. Thus, for clear sky, the aerosol correction is 0. The values in the parentheses in Figure 5 represent the aerosol correction. The aerosol correction for spherical dust is about 2.0–2.5 times that for spheroidal dust. Explicit aerosol correction using spherical dust (Jung et al., 2019; J.-T. Lin et al., 2014, 2015; Martin et al., 2003)
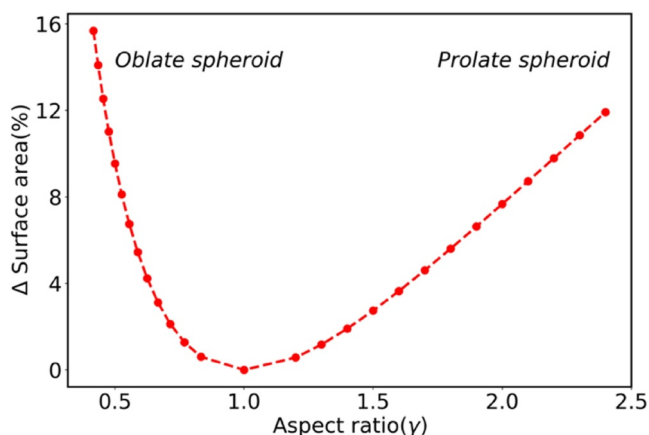
Figure 6. Change in the surface area of spheroidal shape dust particles from spherical shape as a function of aspect ratio.

or implicit aerosol correction treating dust as Mie scattering clouds (Boersma et al., 2011; Bucsela et al., 2006) will overestimate the effect of aerosols as on the AMF.

We also investigated the impact of small surface reflectance (5%), a typical value for the vegetative surfaces at 440 nm, on scattering weights. As expected, the scattering weights and hence, AMF decrease for each viewing geometry for spherical dust, spheroidal dust and clear sky when compared with above results (Appendix D). The overall conclusion remains that accounting for non-sphericity for dust reduces the need to correct for its effects on UV-Vis trace gas retrievals.

5. Dust Shape, Roughness, and Heterogeneous Chemistry

The surface area of an aerosol is a key parameter in estimating the chemical loss of gas to it. We first estimate the change in surface area of a dust particle when deviating from spherical to spheroidal shape before examining effects of surface roughness, and heterogeneous uptake. The approach follows that used in Section 3. Since the surface area of a randomly oriented spheroidal particle is 4 times the projected area, the expression for the ratio of geometric surface areas has the same form as the ratio of geometric projected areas as described in Equations 10 and 11.

$$\frac{\langle S \rangle_{\text{prolate}}}{\langle S \rangle_{\text{sphere}}} = \frac{1}{2\gamma^{\frac{2}{3}}}\left[1 + \frac{\gamma}{e}\sin^{-1}(e)\right] = f(\gamma) \tag{19}$$

$$\frac{\langle S \rangle_{\text{oblate}}}{\langle S \rangle_{\text{sphere}}} = \frac{1}{2\gamma^{\frac{2}{3}}}\left[1 + \frac{1 - e^2}{e}\tanh^{-1}(e)\right] = f(\gamma) \tag{20}$$

Figure 6 shows the change in the surface area of spheroidal dust particles at different aspect ratios. At extreme aspect ratios (0.42 for oblate spheroid and 2.4 for prolate spheroid), the increase in surface area is about 16% for oblate spheroid and about 12% for prolate spheroid.

We simulate the total surface area concentration for the size range 0.1–6.0 μm by assuming the dust particles as either spherical or spheroidal using expressions Equtaions 19 and 20. Figure 7 shows the surface area of dust particles (a) when a spheroidal shape is assumed and (b) the difference when deviating from spherical shape. The surface area calculated for spheroid particles is averaged over the 26 aspect ratios. The distribution of the dust surface area follows that of dust mass with enhancements over arid regions. The spheroidal surface area is about 6% greater than the spherical surface area.

However, dust particles are highly irregular asymmetric particles with a rough surface of microscale structures such as pores, cavities, and capillaries (collectively referred to as pores hereafter). The pores are thought to have a
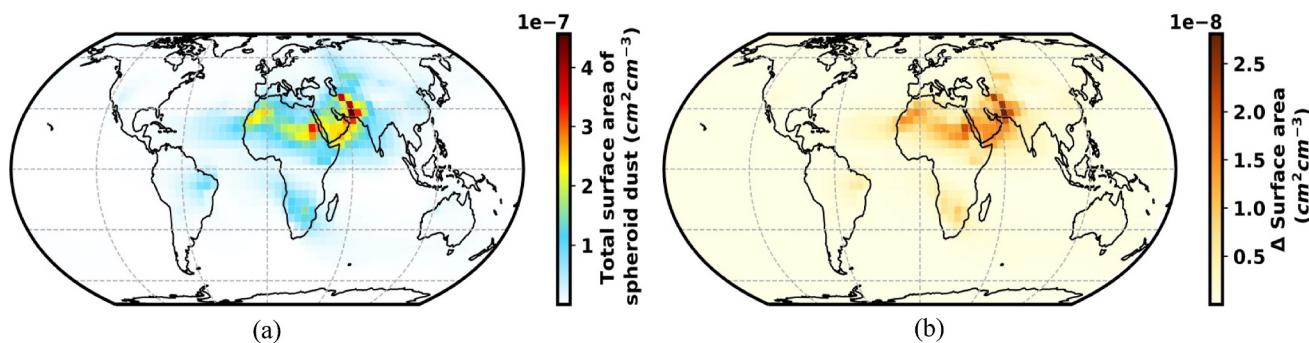
Figure 7. (a) GEOS-chem simulated annual mean total surface area of dust particles in the troposphere for 2017 assuming a spheroidal shape for dust and (b) absolute difference in surface area when deviating from spherical shape (spheroid minus sphere).

slit or wedge-shape with open ends resulting from overlapping of the stacked layer structure of lamellae (Rutherford et al., 1997). Given the challenges of fully representing the complexity of pores, we follow the approach of Marcolli (2014) who uses cylindrical pores to develop conceptual understanding of the vapor condensation in dust pores with extension it to the conical pores (Marcolli, 2020). Other work (David et al., 2019) used cylindrical pores to examine the role of pore condensation and freezing for the ice formation in the atmosphere below water saturation. Therefore, we treat the surface pores as cylindrical structures and assess the surface area change and its effects on heterogeneous chemistry when deviating from smooth to rough particles. We extend the results to conical pores in Appendix G.

It has been shown that the cumulative size distribution of the pores in the porous medium follows a fractal scaling law (Majumdar & Bhushan, 1990; S. Yang et al., 2014; Yu & Cheng, 2002).

$$N(L \geq \rho) = \left(\frac{\rho_{max}}{\rho}\right)^{D_f} \tag{21}$$

where N is the number of pores, L is the length scale, ρ denotes the radius of the pore base, and ρ_{max} denotes the maximum pore base radius, D_f is the surface fractal dimension for dust particles which is within 2–3 (Laaksonen et al., 2016). $D_f = 2$ represents a completely smooth particle and $D_f = 3$ represents a particle surface completely occupied by pores. Differentiating Equation 21 with respect to ρ gives the number of pores whose sizes lie within the range from ρ to $\rho + d\rho$

$$-dN = D_f \rho_{max}^{D_f} \rho^{-(D_f+1)} d\rho \tag{22}$$

The negative sign indicates that pore number decreases with their increasing size as implied by Equation 21. Now, the change in the surface area due to change in number of pores can be calculated as

$$dS_{rough} = dS_{smooth} + (-dN)\, 2\pi\rho h$$

$$d(S_{rough} - S_{smooth}) = (-dN)\, 2\pi\rho h \tag{23}$$

where h is the height of the cylindrical cavity. Substituting Equation 22 into Equation 23 and integrating from ρ_{min} to ρ_{max}, yields

$$(S_{rough} - S_{smooth}) = \pi\rho_{max}^2 \left(\frac{D_f}{D_f - 2}\right) 2\beta \left(\alpha^{D_f-2} - 1\right) \tag{24}$$

Upon rearranging and using $S_{smooth} = 4\pi r^2$, Equation 24 can be written as

$$\frac{S_{rough}}{S_{smooth}} = \frac{1}{4}\left(\frac{\rho_{max}}{r}\right)^2 \left(\frac{D_f}{D_f - 2}\right) 2\beta \left(\alpha^{D_f-2} - 1\right) + 1 \tag{25}$$

where, r is the radius of a spherical particle and equivalent volume radius of a spheroid. Equation 25 gives the relationship between surface area change due to surface roughness, surface fractal dimension and the geometrical parameters ($\alpha = (\rho_{max}/\rho_{min})$ and $\beta = (h/\rho)$) used to model the surface roughness. All terms on the right side of Equation 25 are positive which reflects the increase in surface area of the dust particles due to the increasing surface roughness. Although representative values are unavailable on the geometrical parameter α and β, the surface porosity can be used to constrain these parameters. Surface porosity (ϕ) is a ratio of the total pore volume to the volume of a particle. Using this definition, we obtain

$$\phi = \frac{\int(-dN)\pi\rho^2 h}{\frac{4}{3}\pi r^3} = \frac{3}{4}\left(\frac{\rho_{max}}{r}\right)^3 \beta\left(\frac{D_f}{3 - D_f}\right)\left(1 - \frac{1}{\alpha^{3-D_f}}\right) \tag{26}$$

We define another parameter ε which represents the fractional surface area occupied by the cross-sectional area of pores.

$$\varepsilon = \frac{\int(-dN)\pi\rho^2}{4\pi r^2} = \frac{1}{4}\left(\frac{\rho_{\max}}{r}\right)^2 \left(\frac{D_f}{D_f - 2}\right)\left(\alpha^{D_f - 2} - 1\right) \tag{27}$$

The right sides of Equations 26 and 27 are obtained by substituting the value of $(-dN)$ from Equation 22 and integrating. Comparing Equations 25 and 27, yields

$$\frac{S_{\text{rough}}}{S_{\text{smooth}}} = 2\beta\varepsilon + 1 \tag{28}$$

Again, there is a lack of information on ε. But ε can be related to ϕ using K such that $K = \varepsilon/\phi$. Therefore, we have

$$\frac{S_{\text{rough}}}{S_{\text{smooth}}} = 2\beta K\phi + 1 \tag{29}$$

We assume that β is statistically a constant such that height h and radius ρ follows same fractal law. Therefore, from Equation 21, we have

$$\frac{\rho_{\max}}{\rho} = \frac{h_{\max}}{h}$$

$$\frac{\rho_{\max}}{h_{\max}} = \frac{\rho}{h} = \frac{1}{\beta} \tag{30}$$

We assume that $h_{\max} \ll r$ where $h_{\max}$ is maximum height of a cylindrical cavity in the particle. We use $h_{\max} = 0.15$ to $0.25\ r$ centered around $0.20\ r$ for subsequent analysis. We incorporate the uncertainty in surface area calculation by doing so. We examine the validity of this assumption in Appendix E. From Equation 30, we derive the following relationship

$$\frac{\rho_{\max}}{r} = \frac{0.20}{\beta} \tag{31}$$

Substituting this relation into Equation 26, yields

$$\phi = \frac{3}{4}\frac{(0.20)^3}{\beta^2}\left(\frac{D_f}{3 - D_f}\right)\left(1 - \frac{1}{\alpha^{3-D_f}}\right) \tag{32}$$

The expression for K can be obtained by dividing Equation 27 with Equation 26 and with the help of relation Equation 23 and for $h_{\max} = 0.20r$, yields

$$K = \frac{5}{3}\left(\frac{3 - D_f}{D_f - 2}\right)\left(\frac{\alpha^{D_f - 2} - 1}{\alpha^{3 - D_f} - 1}\right)\left(\alpha^{3 - D_f}\right) \tag{33}$$

We eliminate β from Equation 29 using Equation 32 and substitute the expression for K from Equation 33 to calculate the surface area change with respect to the porosity. We use $D_f = 2.43$, for calcite and $D_f = 2.66$ for quartz dust particles obtained by Laaksonen et al. (2016). Huang et al. (2015) observed that most dust pores are mesopores (2–50 nm). So, we take $\alpha = 15, 20, 25$ to represent the implied ratio. We verify if these values satisfy the normalization condition in Appendix E. Huang et al. (2015) provide total pore volume obtained experimentally for three different types of mineral dust: Asian mineral dust, Tengger desert dust and Arizona test dust of 0.020, 0.016, 0.023 cm^3/g respectively. The specific volume of the mineral dust is 0.38 cm^3/g for the bulk density of mineral dust of 2.65 g/cm^3. The resultant porosities obtained for the three different mineral dust types are 0.053, 0.04 and 0.06. So, we fix the upper limit of porosity to 6%.

The top row of Figure 8 shows the change in surface area due to roughness elements. The surface area of rough particles is increased with respect to smooth particles by about 17%–82% (20%–78% for conical pores with same volume as cylindrical pores (Appendix G, Figure G1)) depending on the porosity of the particle, surface fractal
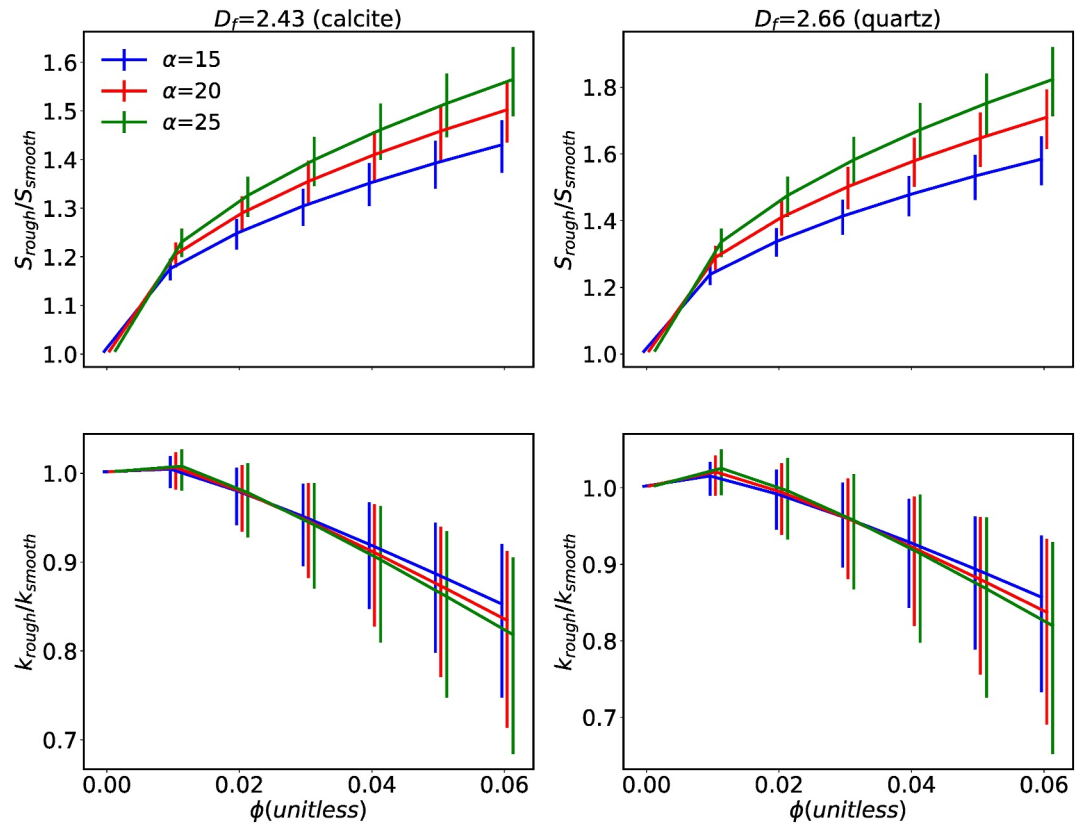
Figure 8. (top) Surface area change due to the presence of roughness elements (pores) for a dust particle as a function of porosity. (bottom) Ratio of rate constant of rough particles (k_{rough}) to the rate constant of smooth particles (k_{smooth}) as a function of porosity. The ratio is calculated for $\eta = 0.28$. Colors indicate the ratio of maximum to minimum pore radius (α). Solid lines represent $h_{\max} = 0.20\,r$. Error bars represent the variation in dependent variables when $h_{\max}$ varies from 0.15 to 0.25 r.

dimension and ratio of maximum to minimum pore radius (α). Error bars indicate the change in surface area when $h_{\max}$ is varied from 0.15 to 0.25 r.

We next examine how particle roughness affects the diffusion coefficient and heterogeneous uptake. The first order heterogeneous loss rate for a gas molecule with mean molecular speed ν, mean free path σ and gas phase diffusion coefficient D_g on a spherical aerosol of radius r is given by

$$k = \left(\frac{r}{D_g} + \frac{4}{\nu\chi}\right)^{-1} S; \; D_g = \frac{1}{3}\sigma\nu \tag{34}$$

where χ is the reactive uptake coefficient and defined as the probability that a molecule impacting the particle surface undergoes irreversible reaction (Jacob, 2000). r can be defined as the effective radius for the aerosol size distribution, and for spheroids r can be equivalent volume radius. S is the surface area of the aerosol particle per unit volume of air. The rate constant k may be limited by either free molecule collision ($4/\nu\chi$ term in Equation 34) or by diffusion (r/D_g term).

For pores, the diffusion coefficient or effective diffusivity (Aris, 1989) is given by

$$D_e = \frac{\phi}{\psi}D_k, \; D_k = \frac{2}{3}\rho_{\text{avg}}\nu \tag{35}$$

where ψ is tortuosity of the particle, D_k is the Knudsen diffusion coefficient that accounts for diffusion into the pores with size less than mean free path, and ρ_{avg} is average pore radius which can be defined as the ratio of total

pore volume to the total pore surface area. Typically, ψ is 1–4 for mineral dust (Huang et al., 2015). Equation 35 can be written as

$$\frac{D_e}{D_g} = \frac{\phi}{\psi}\frac{D_k}{D_g} = \frac{\phi}{\psi}\frac{2\rho_{avg}}{\sigma} \tag{36}$$

The average pore diameter ($2\rho_{avg}$) for mesopores with aforementioned cumulative size distribution function is typically at least 10 times smaller than the mean free path of the molecules and with given ranges of porosity and tortuosity, $D_e/D_g \sim O(10^{-3})$. Thus, resistance to the diffusion mass transfer into the pores is high compared to gas phase diffusion. This means that not all the internal surface area will participate in the reaction. The hindrance of gas diffusion to the pores reduces the internal surface area available for the reaction by a factor η known as effectiveness factor (Huang et al., 2015) (Appendix E), which is the fraction of internal surface area participating in the reaction. The heterogeneous loss rate (k) of a gas molecule over rough surfaces k_{rough} can, therefore, be modeled by adding pores to smooth particles and then, correcting for pore diffusion. Thus, k_{rough} can be expressed as function of the rate constant for spherical smooth particles k_{smooth} commonly used in the models.

$$\frac{k_{smooth}}{S_{smooth}} = \frac{k_{rough}}{S_{external} + \eta S_{internal}} \tag{37}$$

which can be expressed as

$$k_{smooth}/S_{smooth} = k_{rough}/\left(\begin{array}{c} S_{smooth} - \int (-dN)\pi\rho^2 + \\ \eta\left(\int (-dN)\,2\pi\rho^2\beta + \int (-dN)\pi\rho^2 \right) \end{array} \right) \tag{38}$$

combining terms yields

$$\frac{k_{smooth}}{S_{smooth}} = k_{rough}/\left(S_{smooth} + (2\eta\beta + \eta - 1) \int (-dN)\pi\rho^2 \right) \tag{39}$$

Using the definition of porosity, Equation 39 reduces to following form.

$$\frac{k_{rough}}{k_{smooth}} = 1 + (2\eta\beta + \eta - 1)\,K\phi \tag{40}$$

Equation 40 can be used calculate the ratio of the rate constant of the rough particle for a given η. Figure 8 (bottom) shows the rate constant change versus porosity for an example acidic uptake of SO_2 ($\eta = 0.28$) by the surface of Asian mineral dust (Huang et al., 2015), mainly composed of quartz and calcite (Liu et al., 2022). The rate constant for $h_{max} = 0.20\ r$ changes by a factor of 1.02–0.82 (initial slight increase and then decrease) depending on the porosity, the surface fractal dimension and ratio of maximum to minimum pore radius (α). Decreasing h_{max} from 0.20 to 0.15 r results in small β. This suggests a decrease in the availability of internal surface area which results in a lower value of k_{rough} as implied by Equation 37. Using conical pores with $h_{max} = 0.60\ r$ changes the rate constant by a factor of 1.01–0.81 (Appendix G, Figure G1)).

The initial increase in k_{rough} (Figure 8 (bottom)) suggests an increase in the internal surface area available for reaction at a given effectiveness factor (η). The decrease in k_{rough} at subsequent porosities suggests that decrease in external surface area outweighs the increase in available internal surface area dictated by η. This prompts an examination of the behaviour of Equation 37 for the limits of η. As $\eta \longrightarrow 0$, k_{rough} decreases with porosity as $S_{external}$ decreases because of addition of pores (Figure F1). $\eta \longrightarrow 0$ describes the limit in which all reactions occur on the surface of the particle which can only be possible if the chemical species is extremely reactive. In such case, the characteristic reaction time scale is very small compared to characteristic diffusion time scale which results in large Thiele modulus (Appendix E) and hence, low effectiveness factor. However, as η approaches unity
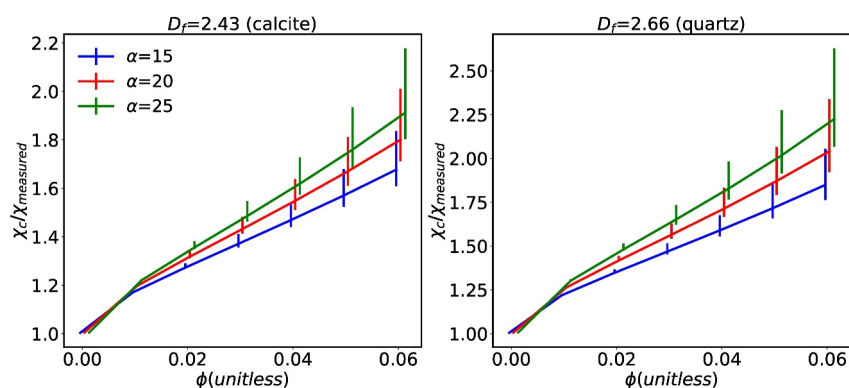
Figure 9. Ratio of corrected uptake coefficient (χ_c) to the measured uptake coefficient ($\chi_{measured}$) as a function of porosity. The ratio is calculated for $\eta = 0.28$. Colors indicate the ratio of maximum to minimum pore radius (α). Solid lines represent $h_{max} = 0.20\ r$. Error bars represent the variation in dependent variables when h_{max} varies from 0.15 to 0.25 r.

(represents the limit case of a non-reactive species filling all pores), k_{rough} increases with porosity as more surface is available for reaction (Figure F2). This suggests a presence of critical η where

$$S_{smooth} = S_{external} + \eta_{crit} S_{internal} \tag{41}$$

which, upon simplification, gives

$$\eta_{crit} = \frac{1}{2\beta + 1} \tag{42}$$

Figure F3 shows the rate constant change versus η for smooth particles corrected for pore diffusion. Varying η from 0 to 1 spans the range of possible chemical interactions with dust particles in the atmosphere. The points where curves intersect the dashed line represent the critical η. At these points, k_{rough} starts increasing with respect to k_{smooth}.

The theoretical model developed until now explains how the surface area and rate constant change when adding pores to a smooth particle keeping the reactive uptake coefficient constant. However, in experimental studies (Hanisch & Crowley, 2001; Huang et al., 2015) where dust is already considered porous or rough, one needs to study the behavior of the reactive uptake coefficient (χ) used in rate constant formulation (34). The reactive uptake coefficient (χ) is calculated based on the entire surface area of a real particle with pores and should be corrected for the pore diffusion. To do so, Equation 37 can be modified to the following form.

$$\chi_{measured} S_{rough} = \chi_c \left(S_{external} + \eta S_{internal} \right) \tag{43}$$

Here, χ_c is uptake coefficient corrected for the internal surface area available for reaction. By applying a similar mathematical approach as Equations 37–40 and 43 can be further reduced to

$$\frac{\chi_{measured}}{\chi_c} = \left(\frac{S_{smooth}}{S_{rough}} + \frac{(2\eta\beta + \eta - 1)\,K\phi}{(2\beta\phi K + 1)} \right) \tag{44}$$

Figure 9 shows the reactive uptake coefficient change versus porosity for acidic uptake of SO_2 ($\eta = 0.28$) by the rough surface (particle with pores) of Asian mineral dust (Huang et al., 2015). The corrected reactive uptake for $h_{max} = 0.20\ r$ is increased by a factor of about 1.2–2.2 depending on the porosity, the surface fractal dimension and ratio of maximum to minimum pore radius (α). The corrected reactive uptake for conical pores with $h_{max} = 0.60\ r$ is increased by factor of about 1.2–2.2 (Appendix G, Figure G2). Correcting for pore diffusion in a real particle always reduces the available internal surface area for reaction.

We extend the above result for SO_2 to span the range of possible chemical interactions with dust particles in the atmosphere (Appendix F, Figure F4). Figure F4 shows the reactive uptake coefficient change with respect to effectiveness factor with $\phi = 0.05$. The ratio of corrected reactive uptake coefficient to measured reactive uptake coefficient decreases with effectiveness factor. For non-reactive species ($\eta = 1$), the ratio is always unity. For highly reactive species (η nearly equal to zero), the ratio depends on surface fractal dimension (D_f) and ratio of maximum to minimum pore radius (α). The maximum ratio is about 3.4 for $D_f = 2.66$ and $\alpha = 25$ (calculated for $h_{max} = 0.20\ r$). The value of η for an example species is 0.03 (Hanisch & Crowley, 2001) for HNO_3 yields a range of corrected uptake 1.9–3.1 (for 5% porosity).

Limitations: The theoretical model used here is based on cylindrical and conical pore shape following recent practice (David et al., 2019; Marcolli, 2014, 2020) despite expectation that real dust contains slit or wedge-shaped pores with open ends (Rutherford et al., 1997). Future work should explore ways to mathematically incorporate wedge shape pores. Another limitation arises from β being treated as statistically constant. The depth of the pore (h) may follow different scaling laws with different fractal dimension in natural settings. It should also be noted that the current theoretical framework is for pure dust. A chemical coating of condensed gases on the aged dust surface may affect porosity, surface area, and the reactive uptake coefficient. Pan et al. (2017) observed that depolarization ratio of aged dust over Beijing decreases implying that dust particles tend to become spherical (termed as quasi-spherical) in a polluted environment, therefore affecting the surface area. The uptake coefficient of the aged dust may also depend on hygroscopicity of the coated dust. The weakly hygroscopic nature of some coatings such as $CaSO_4$ can limit further uptake of water-soluble gases whereas, more hygroscopic coating such as $Ca(NO_3)_2$ can promote the formation of hydration layer and enhance of the reactive uptake of acidic gases (Fairlie et al., 2010; Heim et al., 2020). Future work is needed to further examine these processes in chemical transport models.

6. Summary and Conclusion

Mineral dust is often treated as spherical in chemical transport models and in solar backscatter retrievals of trace gases. Although the effects of dust shape upon aerosol retrievals have been extensively examined, knowledge gaps remain of their effects upon chemical transport model simulations and trace gas retrievals. We investigate the effects of dust morphology on aerosol optical properties and aerosol surface area, diffusion and reaction parameters used in chemical transport models, and radiance and scattering weights for AMF calculations in solar backscatter retrievals. Spheroids with different aspect ratios are used to model the dust phase function with an equiprobable mixture of prolate and oblate spheroids. We find that the extinction efficiency can differ significantly (>10%) when using spheroidal shapes to model submicron dust. The aggregate change in optical depth across submicron size dust particles is within 5% which may be important for some applications.

To our knowledge, all prior studies of the effects of aerosols on UV-Vis solar backscatter retrievals of trace gases have treated dust as spherical. We first examined scattered radiance and find an 18% increase in forward scattering and a 21% decrease in backscattering when using spheroidal rather than spherical dust. We find that the increased forward scattering from spheroidal rather than spherical dust increases the transmission of the solar beam into the dust layer, thus leading to an increase in scattering weights near the surface due to more "clear sky" like behavior. The effect of aerosols on scattering weights and AMF of NO_2 is thus weaker by roughly factors of 2.0–2.5 for variety of test scenarios over the dusty region of Riyadh when using spheroidal rather than spherical dust.

We examined knowledge gaps of dust non-sphericity upon surface area for heterogeneous chemistry in chemical transport models. We begin with surface area calculations by treating dust as spheroidal particles. The surface area increase introduced by spheroidal rather than spherical particles is about 6% when averaged over various aspect ratios. We subsequently examined the effect of dust surface roughness on surface area. We derived a novel equation that relates surface area change due to surface roughness to the surface fractal dimension and porosity. We found that surface roughness could increase surface area by factors of 1.2–1.8 with pronounced sensitivity to fractal dimension and dust porosity which in turn, affects the rate constant. We found that species reactivity plays an important role in determining the rate constant for rough particles along with surface area. In addition, we studied the impact of surface roughness on gaseous reactive uptake and diffusivity. We found that corrected reactive uptake is a function of surface area, porosity, and effectiveness factor whereas

corrected diffusivity is a function of porosity and tortuosity. The uptake coefficient is increased under the influence of surface roughness and change in surface area. We found that surface area and subsequently, heterogeneous chemistry is more affected by dust surface irregularities rather than shape of the particles.

Overall, we find sufficient importance of the impact of non-sphericity of dust particles on simulated extinction, AOD, phase function, radiance and scattering weights to warrant inclusion in chemical transport models and UV-Vis trace gas retrievals. Future work could consider superspheroids that uses an roundness parameter along with size and aspect ratio to characterize the shape (W. Lin et al., 2018) or ellipsoids with three degrees of freedom with different shape distribution function (e.g., Gaussian rather than equiprobable mixture of shapes) to model the optical parameters of the dust particles. Since T-matrix method has some limitations, machine learning techniques could be useful in generating look up table of the dust optical properties in future. The effects of dust non-sphericity on heterogeneous chemistry calculations in chemical transport models is however too uncertain to confidently represent at this time. Future work should attempt to further constrain the extent of its effect. Super coarse dust with diameter greater than 10 μm is gaining attention as an important contribution to dust mass (Ryder et al., 2018; Varga et al., 2021); further development of CTMs is needed to represent this coarse mode (Meng et al., 2022).

Appendix A
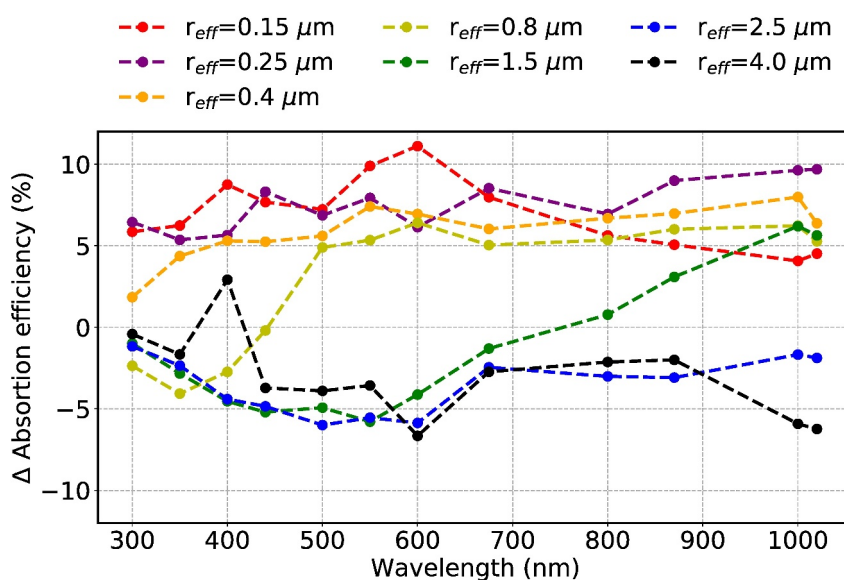
Figure A1. Relative difference in absorption efficiency $\left(\frac{(Q_{abs,\text{sphere}} - Q_{abs,\text{spheroid}}) * 100}{Q_{abs,\text{sphere}}}\right)$ versus wavelength.

Table A1
Aspect Ratios at Which the T-Matrix Code Converges for Different Range of Size Parameters

Size parameter	Aspect ratios
0–35	0.41–2.6 (26 aspect ratios)
35–40	0.45–2.2 (24 aspect ratios)
40–50	0.62–2.0 (16 aspect ratios)
50–60	0.71–1.8 (11 aspect ratios)
60–80	0.83–1.4 (4 aspects ratios)

Note. We use 26 aspect ratios ranging from 1.2 to 2.4 (prolate spheroid) with a step size of 0.1 for prolate spheroids and the inverse of these values for oblate spheroids following the approach of Mishchenko et al. (1997).

Table A2.

Table A2
Log-Normal Distribution Parameters Used for Different Size Bins

Size range	r_g^a	σ_g^b	r_{eff}^c	v_{eff}^d
0.1–0.18	0.5	2.2	0.15	0.019
0.18–0.3	0.5	2.2	0.25	0.017
0.3–0.6	0.09	2.2	0.40	0.037
0.6–1.0	0.5	2.2	0.80	0.02
1.0–1.8	4.0	2.2	1.49	0.02
1.8–3.0	4.0	2.2	2.49	0.018
3.0–6.0	0.09	2.2	3.72	0.03

[a]Geometric radius; [b]Geometric standard deviation; [c]Effective radius; [d]effective variance $= \frac{1}{\langle G \rangle r_{eff}^2} \int_{r_{min}}^{r_{max}} dr \, n(r) \, (r - r_{eff})^2 \pi r^2$.
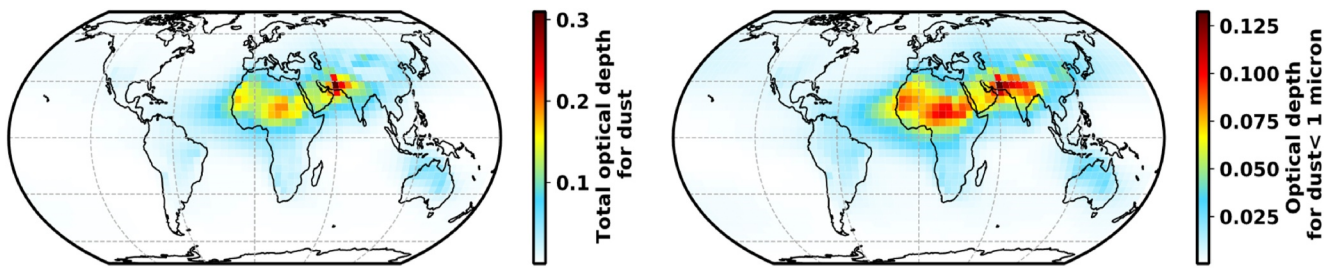
Appendix B

Figure B1. Annual mean (a) total spherical dust AOD (b) sub-micron spherical dust AOD for the year of 2017 simulated at 550 nm.
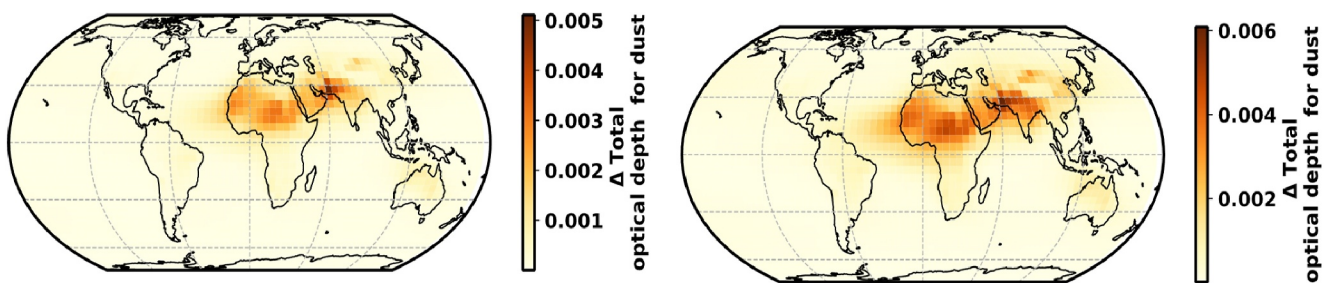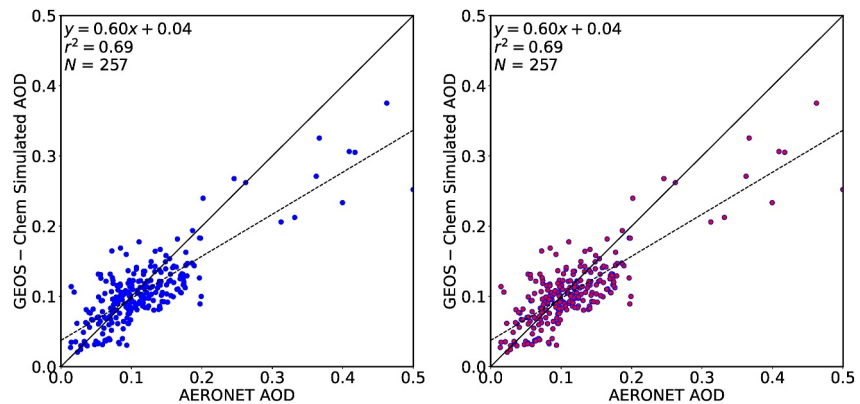

Figure B2. Differences (Δ, Sphere-Spheroid) in monthly mean (a) total dust AOD (b) sub-micron dust AOD for the year of 2017 simulated at 550 nm.

Figure B3. Comparison between GEOS-Chem simulated annual mean AOD (2017) and AERONET AOD. Blue circles represent GEOS-Chem simulated total AOD with spherical dust colocated at AERONET sites while pink circles represent GEOS-Chem simulated total AOD with spheroidal dust colocated at AERONET sites. The solid line represents $y = x$ and dashed line represents regression line.

Appendix C

We retain the effective radii (Table C1) used for standard gamma distribution in Table C2 and Table C3. The refractive index used in all the tables is $1.558 + 0.0014i$ (Sinyuk et al., 2003). ω is single scattering albedo, λ is wavelength (in nm), r_{eff} is effective radius (in μm), Q_{ext} is extinction efficiency, and $\pi(0-7)$ are first eight expansion coefficients of the phase function. Table C4 describes the spectral refractive indices at different wavelengths.

Table C1
Default Look up Table of the Optical Properties for Spherical Particles at 550 nm Assuming Standard Gamma Distribution in GEOS-Chem

Default										
r_{eff}	Q_{ext}	ω	$\pi(0)$	$\pi(1)$	$\pi(2)$	$\pi(3)$	$\pi(4)$	$\pi(5)$	$\pi(6)$	$\pi(7)$
0.15	1.574	0.993	1.000	1.766	1.248	0.460	0.143	0.027	0.003	0.000
0.25	3.624	0.994	1.000	2.101	2.473	2.097	1.416	0.769	0.355	0.076
0.40	3.642	0.990	1.000	2.005	2.702	2.636	2.714	2.500	2.179	1.787
0.82	2.623	0.971	1.000	2.142	3.213	3.457	4.381	4.388	4.957	4.747
1.49	2.368	0.953	1.000	2.256	3.339	3.617	4.635	4.902	5.843	6.053
2.42	2.270	0.930	1.000	2.357	3.499	3.897	4.971	5.373	6.463	6.862
3.72	2.125	0.897	1.000	2.409	3.562	4.009	5.070	5.556	6.708	7.235

Table C2
Revised Look up Table of the Optical Properties for Spherical Particles at 550 nm Assuming Log-Normal Distribution

Revised (spheres)										
r_{eff}	Q_{ext}	ω	$\pi(0)$	$\pi(1)$	$\pi(2)$	$\pi(3)$	$\pi(4)$	$\pi(5)$	$\pi(6)$	$\pi(7)$
0.15	1.559	0.993	1.000	1.763	1.243	0.457	0.142	0.026	0.003	0.000
0.25	3.589	0.994	1.000	2.097	2.456	2.070	1.383	0.740	0.339	0.073
0.42	3.385	0.989	1.000	1.949	2.608	2.450	2.505	2.217	1.893	1.517
0.80	2.544	0.971	1.000	2.086	3.121	3.284	4.188	4.148	4.722	4.495
1.49	2.268	0.950	1.000	2.229	3.261	3.456	4.380	4.536	5.402	5.553
2.49	2.230	0.927	1.000	2.355	3.480	3.857	4.893	5.279	6.360	6.775
3.72	2.154	0.899	1.000	2.412	3.575	4.036	5.111	5.608	6.767	7.295

Table C3
Revised and Final Look up Table of the Optical Properties for Spheroidal Particles at 550 nm Assuming Log-Normal Distribution

r_{eff}	Q_{ext}	ω	$\pi(0)$	$\pi(1)$	$\pi(2)$	$\pi(3)$	$\pi(4)$	$\pi(5)$	$\pi(6)$	$\pi(7)$
Revised (spheroids)										
0.15	1.382	0.993	1.000	1.763	1.305	0.553	0.193	0.047	0.009	0.001
0.25	3.287	0.994	1.000	2.129	2.432	2.113	1.478	0.822	0.403	0.139
0.42	3.436	0.990	1.000	2.058	2.718	2.918	2.885	2.644	2.297	1.874
0.80	2.377	0.970	1.000	1.910	2.769	3.175	3.591	3.773	4.021	4.123
1.49	2.299	0.948	1.000	2.136	3.177	3.830	4.484	4.934	5.483	5.928
2.49	2.215	0.922	1.000	2.224	3.338	4.134	4.921	5.547	6.268	6.923
3.72	2.168	0.896	1.000	2.266	3.522	4.354	5.139	5.858	6.746	7.551

Table C4
Spectral Refractive Index of Dust Particles Following Sinyuk et al. (2003)

| Wavelength (λ) (in nm)	Refractive index	Wavelength (λ) (in nm)	Refractive index
300	$1.6 + 0.0087\,i$	600	$1.553 + 0.0011\,i$
350	$1.58 + 0.0058\,i$	675	$1.5278 + 0.004597\,i$
400	$1.58 + 0.0036\,i$	800	$1.53 + 0.004\,i$
440	$1.5756 + 0.00276\,i$	870	$1.5301 + 0.004265\,i$
500	$1.564 + 0.0018\,i$	1,000	$1.53 + 0.001\,i$
550	$1.558 + 0.0014\,i$	1,020	$1.53 + 0.00067\,i$

Appendix D

Figure D1.
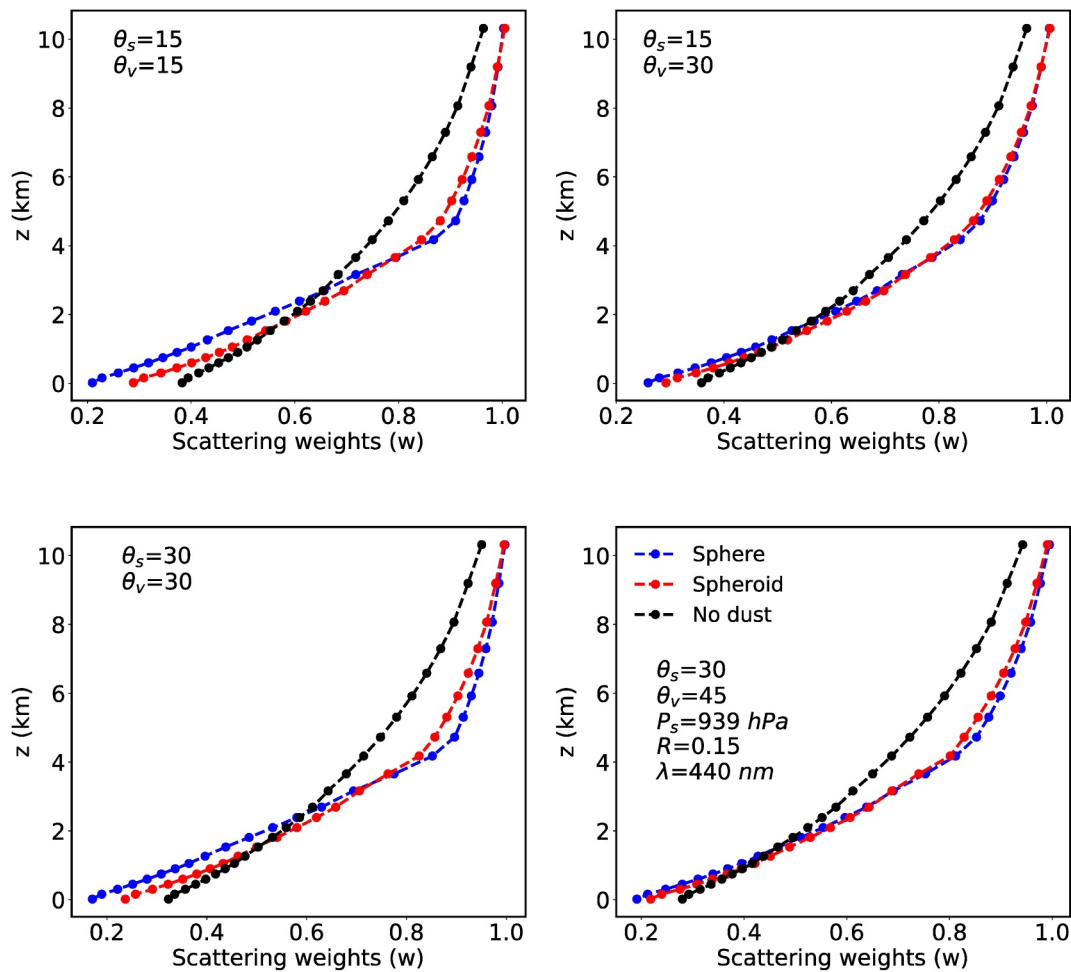
Figure D1. Scattering weights for the atmosphere below 10 km with dust ($\tau_{440} = 0.3$) uniformly distributed up to 4 km for 4 different viewing geometries. Scattering weights are calculated for wavelength (λ) of 440 nm, surface pressure (P_s) of 939 hPa and Lambertian surface reflectance (R) of 0.05.

Figure D2.
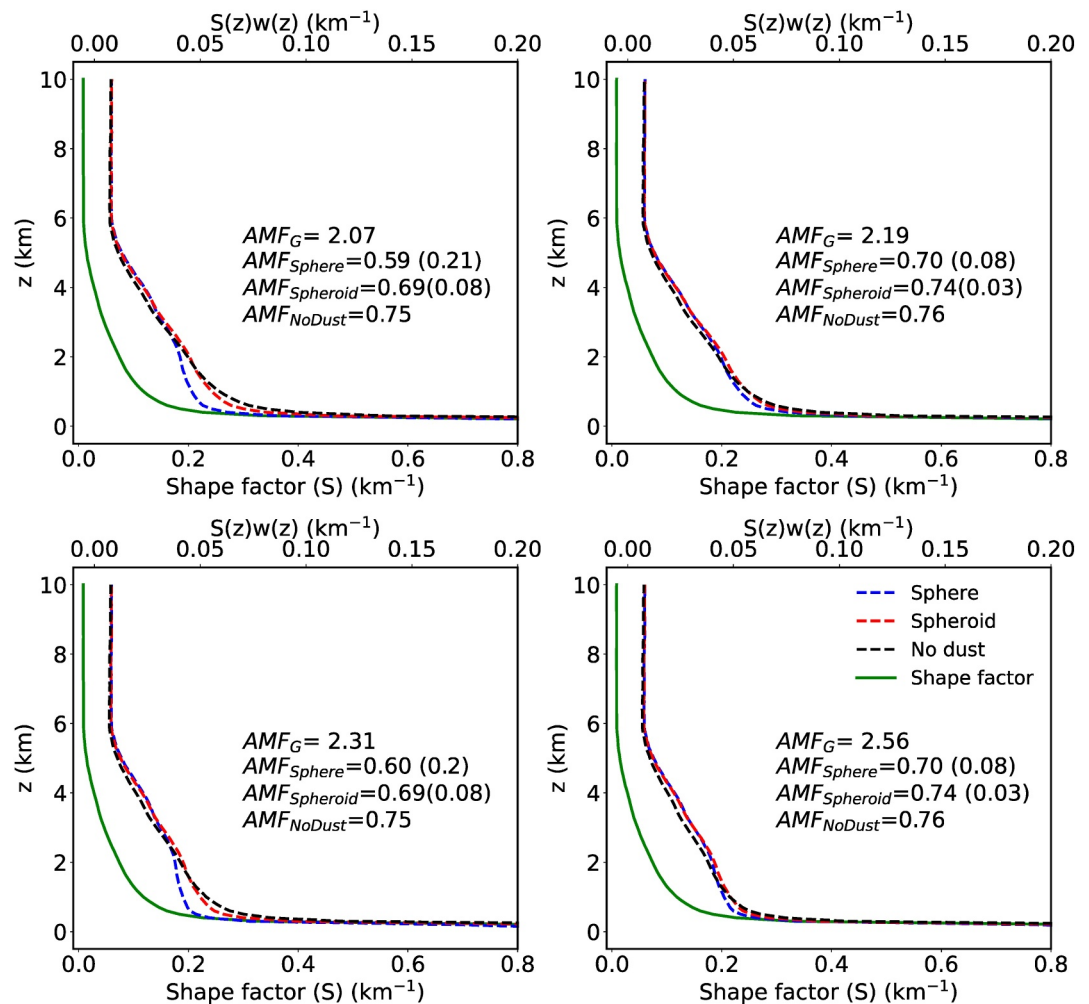
Figure D2. GEOS- Chem simulated monthly mean vertical shape factor (S) (solid black line) for NO_2 as a function of height z over Riyadh, Saudi Arabia. The blue, red and green lines represent the product $w(z)S(z)$, for spherical, spheroidal dust and clear sky, respectively. Values of air mass factor (AMF) calculated assuming spherical and spheroidal dust are also shown along with geometrical AMF (AMF_G) and clear sky AMF. Values in parentheses are the aerosol correction.

Appendix E

The left-hand side of Equation 29 can be rewritten as following.

$$\frac{S_{\text{rough}}}{S_{\text{smooth}}} = \frac{S_{\text{external}}}{S_{\text{smooth}}} + \frac{S_{\text{internal}}}{S_{\text{smooth}}} \tag{E1}$$

which can be expressed as

$$\frac{S_{\text{rough}}}{S_{\text{smooth}}} = \frac{S_{\text{smooth}} - \int(-dN)\pi\rho^2}{S_{\text{smooth}}} + \frac{\int(-dN)\,2\pi\rho^2\beta + \int(-dN)\pi\rho^2}{S_{\text{smooth}}} \tag{E2}$$

Using the definition of ε, yields

$$\frac{S_{\text{rough}}}{S_{\text{smooth}}} = (1 - K\phi) + (2\beta + 1) K\phi \tag{E3}$$

The first term of the right-hand side describes the fractional decrease in the external surface area and second term indicates the fractional increase in the internal surface area when we add pores to a smooth surface. Since fractional decrease in the external surface area cannot be equal to or less than zero, we obtain a following condition where,

$$K\phi < 1 \tag{E4}$$

The assumed range of h_{max} satisfies this condition for a given range of D_f, α and ϕ.

E1. Pore Distribution Function and Normalization Condition

The fractal scaling law for pore distribution is

$$N(L \geq \rho) = \left(\frac{\rho_{\text{max}}}{\rho}\right)^{D_f} \tag{E5}$$

Differentiating Equation E5 with respect to give the number of objects whose sizes lie within the range from ρ to $\rho + d\rho$

$$-dN = D_f \rho_{\text{max}}^{D_f} \rho^{-(D_f + 1)} d\rho \tag{E6}$$

From Equation E5, the total number of pores from ρ_{min} to ρ_{max} can be obtained by

$$N_t(L \geq \rho_{min}) = \left(\frac{\rho_{max}}{\rho_{min}}\right)^{D_f} \tag{E7}$$

Dividing Equation E6 by Equation E5 gives

$$-\frac{dN}{N_t} = D_f \rho_{\text{min}}^{D_f} \rho^{-(D_f + 1)} d\rho = f(\rho) \, d\rho \tag{E8}$$

where $f(\rho) = D_f \rho_{\text{min}}^{D_f} \rho^{-(D_f + 1)}$ is the probability density function for pores in the dust particle. This probability density function should satisfy normalization condition.

$$\int_{\rho_{\text{min}}}^{\rho_{\text{max}}} f(\rho) \, d\rho = 1 - \left(\frac{\rho_{\text{min}}}{\rho_{\text{max}}}\right)^{D_f} = 1 \tag{E9}$$

or

$$1 - \left(\frac{1}{\alpha}\right)^{D_f} = 1 \tag{E10}$$

Substituting $\alpha = 15, 20, 25$ for $2 < D_f < 3$ satisfy Equation E10. Hence, $\alpha = 15, 20, 25$ are valid values for analysis.

E2. Effectiveness Factor

The effectiveness factor can be thought of as a measure of the intraparticle diffusional resistance to the heterogeneous reaction taking place on a porous surface. It is a function of another parameter known as the Thiele modulus (Φ) (Ramachandran, 2014), that is, the ratio of the characteristic time for diffusion (r^2/D_c) to the time for reaction ($1/k$) and for nonspherical particles, it can be written as
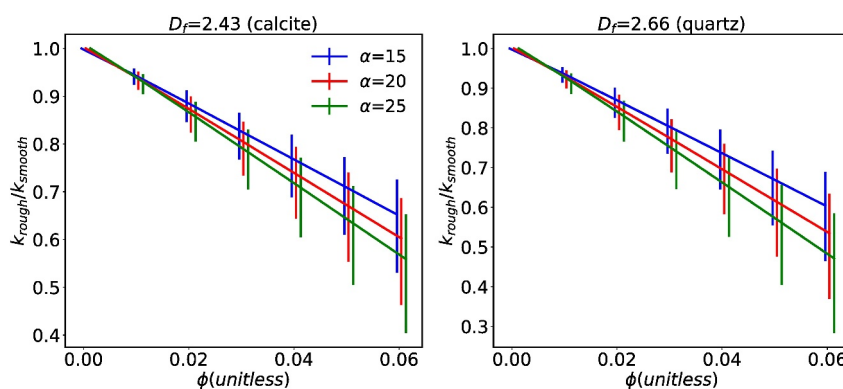
$$\eta = \frac{1}{\Phi}\left[\frac{1}{\tanh(3\Phi)} - \frac{1}{3\Phi}\right] \tag{E11}$$

$$\Phi = r\sqrt{\frac{k}{D_e}} \tag{E12}$$

where r is the equivalent volume radius for nonspherical particles. The dependence of Φ on rate constant (k) makes Equation 28 implicit and can be solved iteratively for χ_c if χ_{measured} is known.
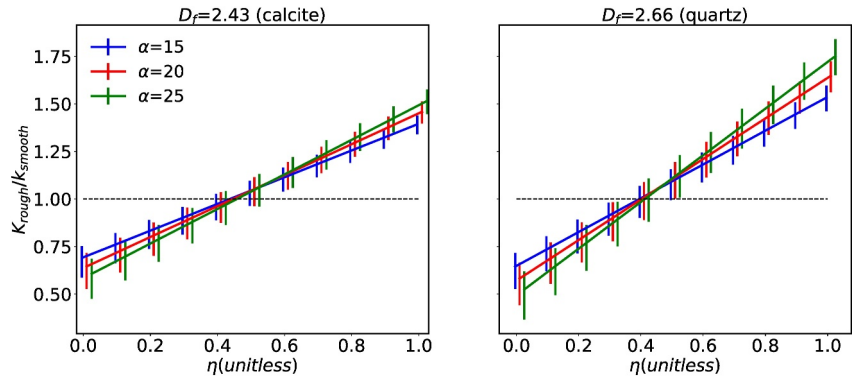
Appendix F

Figure F1. Ratio of rate constant for rough particles (k_{rough}) to the rate constant of smooth particle (k_{smooth}) as a function of porosity. The ratio is calculated for $\eta = 0.03$. Colors indicate the ratio of maximum to minimum pore radius (α). Solid lines represent $h_{\text{max}} = 0.20\ r$. The error bars represent the variation in dependent variables when h_{max} varies from 0.1 to 0.2 r.
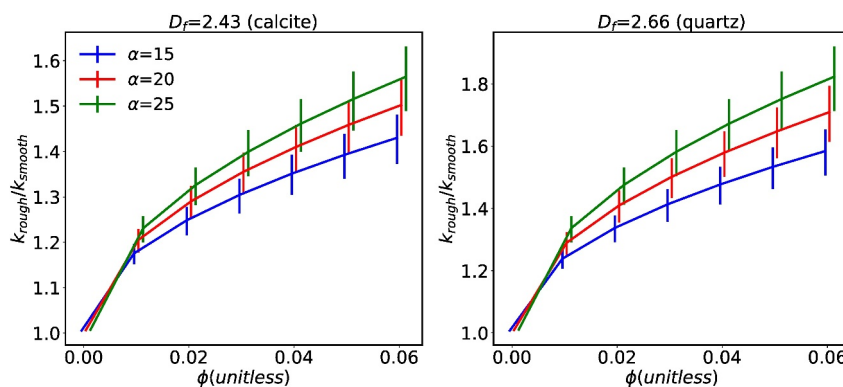
Figure F2. Same as Figure G1 except $\eta = 1.0$.

Figure F3. Ratio of rate constant for rough particles (k_{rough}) to the rate constant of smooth particle (k_{smooth}) as a function of effectiveness factor η. The ratio is calculated for $\phi = 0.05$. Dashed line represents ratio (k_{rough}/k_{smooth}) = 1. Intersection points of dashed line with curves represent critical eta (η_{crit}) values.
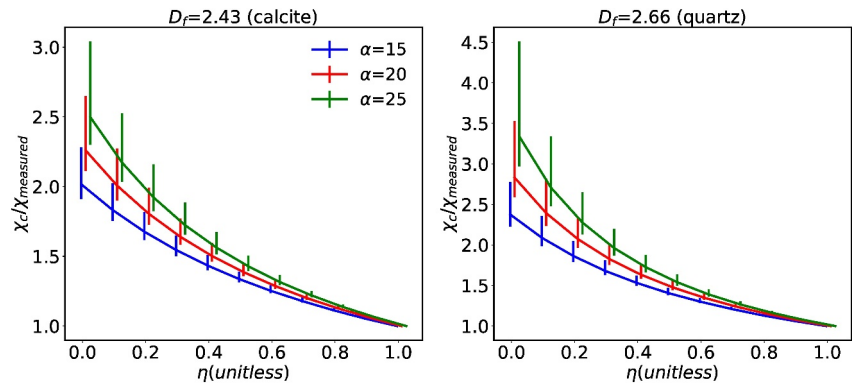
Figure F4. Ratio of corrected uptake coefficient (χ_c) to the measured uptake coefficient ($\chi_{measured}$) as a function of effectiveness factor (η). The ratio is calculated for $\phi = 0.05$. Colors indicate the ratio of maximum to minimum pore radius (α). Solid lines represent $h_{max} = 0.20r$. The error bars represent the variation in dependent variables when h_{max} varies from 0.15 to 0.25 r.

Appendix G

For conical pores, h_{max} varies from 0.45 to 0.75 r centered around 0.60 r, to keep the volume of conical pores to the same as for cylindrical pores (Table G1).

Table G1

Key Formulas Describing the Change in Surface Area and Subsequent Chemistry Changes if We Replace Cylindrical Capillaries With Conical Pores

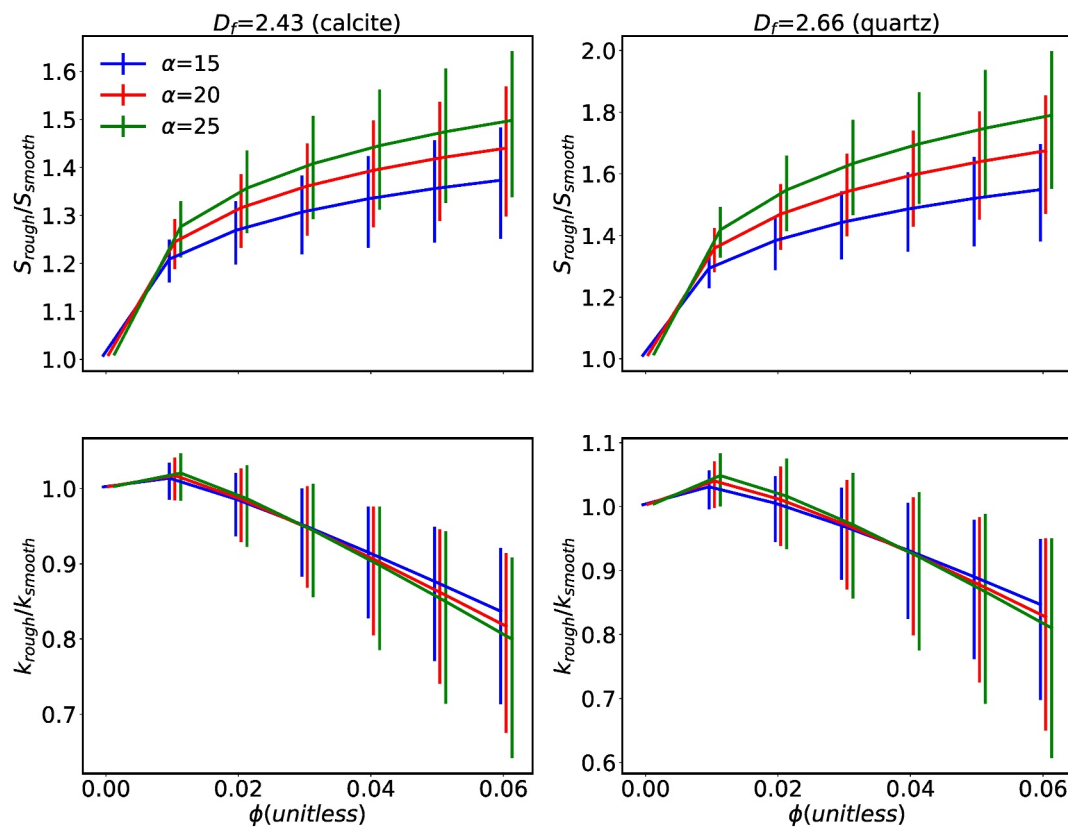| Change in surface area	Relation between ϕ and β
$\frac{S_{rough}}{S_{smooth}} = \left(\sqrt{1+\beta^2} - 1\right)K\phi + 1$	$\phi = \frac{1}{4}\frac{(0.60)^3}{\beta^2}\left(\frac{D_f}{3-D_f}\right)\left(1 - \frac{1}{\alpha^{3-D_f}}\right)$
where, $K = 1.67\left(\frac{3-D_f}{D_f-2}\right)\left(\frac{\alpha^{D_f-2}-1}{\alpha^{3-D_f}-1}\right)(\alpha^{3-D_f})$	
Change in rate constant	**Change in reactive uptake coefficient**
$\frac{k_{rough}}{k_{smooth}} = 1 + \left(\eta\sqrt{1+\beta^2} - 1\right)K\phi$	$\frac{\chi_{measured}}{\chi_c} = \left(\frac{S_{smooth}}{S_{rough}} + \frac{\left(\eta\sqrt{1+\beta^2}-1\right)K\phi}{\left(\sqrt{1+\beta^2}-1\right)K\phi+1}\right)$
and critical η, $\eta_{crit} = \frac{1}{\sqrt{1+\beta^2}+1}$	

Figure G1. (top) Surface area change due to the presence of roughness elements (conical shape pores) for a dust particle as a function of porosity. (bottom) Ratio of rate constant of rough particles (k_{rough}) to the rate constant of smooth particles (k_{smooth}) as a function of porosity. The ratio is calculated for $\eta = 0.28$. Colors indicate the ratio of maximum to minimum pore radius (α). Solid lines represent $h_{max} = 0.60\ r$. Error bars represent the variation in dependent variables when h_{max} varies from 0.45 to 0.75 r.
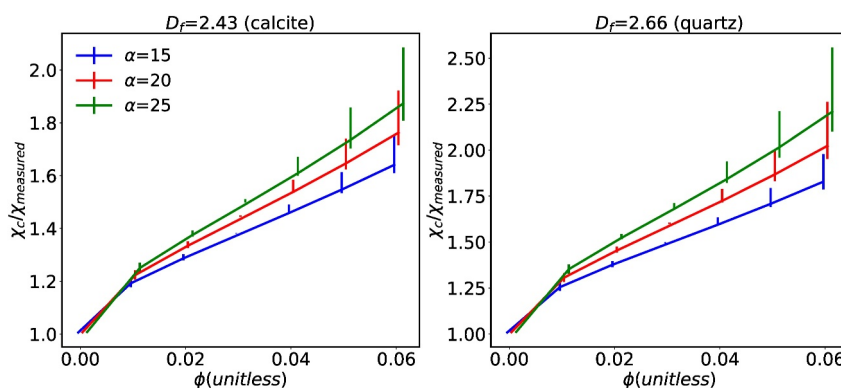
Figure G2. Ratio of corrected uptake coefficient (χ_c) to the measured uptake coefficient ($\chi_{measured}$) as a function of porosity for conical pores. The ratio is calculated for $\eta = 0.28$. Colors indicate the ratio of maximum to minimum pore radius (α). Solid lines represent $h_{max} = 0.60\ r$. Error bars represent the variation in dependent variables when h_{max} varies from 0.45 to 0.75 r.

Data Availability Statement

All data, codes and python notebooks are archived and freely available at https://doi.org/10.5281/zenodo.10914522 (Singh, 2024). UNL-VRTM model used in this work can be obtained from https://unl-vrtm.org/.

References

Aris, R. (1989). 6—The interaction of chemical and physical rate processes. In R. Aris (Ed.), *Elementary chemical reactor analysis* (pp. 113–155). Butterworth-Heinemann. https://doi.org/10.1016/B978-0-409-90221-1.50012-8

Bey, I., Jacob, D. J., Yantosca, R. M., Logan, J. A., Field, B. D., Fiore, A. M., et al. (2001). Global modeling of tropospheric chemistry with assimilated meteorology: Model description and evaluation. *Journal of Geophysical Research*, *106*(D19), 23073–23095. https://doi.org/10.1029/2001JD000807

Bi, L., & Yang, P. (2014). High-frequency extinction efficiencies of spheroids: Rigorous T-matrix solutions and semi-empirical approximations. *Optics Express*, *22*(9), 10270. https://doi.org/10.1364/OE.22.010270

Bi, L., Yang, P., Kattawar, G. W., & Kahn, R. (2010). Modeling optical properties of mineral aerosol particles by using nonsymmetric hexahedra. *Applied Optics*, *49*(3), 334–342. https://doi.org/10.1364/AO.49.000334

Boersma, K. F., Eskes, H. J., Dirksen, R. J., van der A, R. J., Veefkind, J. P., Stammes, P., et al. (2011). An improved tropospheric NO_2 column retrieval algorithm for the Ozone Monitoring Instrument. *Atmospheric Measurement Techniques*, *4*(9), 1905–1928. https://doi.org/10.5194/amt-4-1905-2011

Bohren, C. F., & Singham, S. B. (1991). Backscattering by nonspherical particles: A review of methods and suggested new approaches. *Journal of Geophysical Research*, *96*(D3), 5269–5277. https://doi.org/10.1029/90JD01138

Bucsela, E. J., Celarier, E. A., Wenig, M. O., Gleason, J. F., Veefkind, J. P., Boersma, K. F., & Brinksma, E. J. (2006). Algorithm for NO/sub 2/ vertical column retrieval from the ozone monitoring instrument. *IEEE Transactions on Geoscience and Remote Sensing*, *44*(5), 1245–1258. https://doi.org/10.1109/TGRS.2005.863715

Cooper, M. J., Martin, R. V., Hammer, M. S., & McLinden, C. A. (2019). An observation-based correction for aerosol effects on nitrogen dioxide column retrievals using the absorbing aerosol index. *Geophysical Research Letters*, *46*(14), 8442–8452. https://doi.org/10.1029/2019GL083673

David, R. O., Marcolli, C., Fahrni, J., Qiu, Y., Perez Sirkin, Y. A., Molinero, V., et al. (2019). Pore condensation and freezing is responsible for ice formation below water saturation for porous particles. *Proceedings of the National Academy of Sciences*, *116*(17), 8184–8189. https://doi.org/10.1073/pnas.1813647116

Dentener, F. J., Carmichael, G. R., Zhang, Y., Lelieveld, J., & Crutzen, P. J. (1996). Role of mineral aerosol as a reactive surface in the global troposphere. *Journal of Geophysical Research*, *101*(D17), 22869–22889. https://doi.org/10.1029/96JD01818

Dubovik, O., Holben, B. N., Lapyonok, T., Sinyuk, A., Mishchenko, M. I., Yang, P., & Slutsker, I. (2002). Non-spherical aerosol retrieval method employing light scattering by spheroids. *Geophysical Research Letters*, *29*(10), 54-1–54-4. https://doi.org/10.1029/2001GL014506

Dubovik, O., Sinyuk, A., Lapyonok, T., Holben, B. N., Mishchenko, M., Yang, P., et al. (2006). Application of spheroid models to account for aerosol particle nonsphericity in remote sensing of desert dust. *Journal of Geophysical Research*, *111*(D11), D11208. https://doi.org/10.1029/2005JD006619

Eskes, H. J., & Boersma, K. F. (2003). Averaging kernels for DOAS total-column satellite retrievals. *Atmospheric Chemistry and Physics*, *7*(5), 1285–1291. https://doi.org/10.5194/acp-3-1285-2003

Fairlie, T., Jacob, D. J., & Park, R. J. (2007). The impact of transpacific transport of mineral dust in the United States. *Atmospheric Environment*, *41*(6), 1251–1266. https://doi.org/10.1016/j.atmosenv.2006.09.048

Fairlie, T. D., Jacob, D. J., Dibb, J. E., Alexander, B., Avery, M. A., van Donkelaar, A., & Zhang, L. (2010). Impact of mineral dust on Nitrate, Sulfate, and Ozone in transpacific Asian pollution plumes. *Atmospheric Chemistry and Physics*, *10*(8), 3999–4012. https://doi.org/10.5194/acp-10-3999-2010

Formenti, P., Elbert, W., Maenhaut, W., Haywood, J., & Andreae, M. O. (2003). Chemical composition of mineral dust aerosol during the Saharan Dust Experiment (SHADE) airborne campaign in the Cape Verde region, September 2000. *Journal of Geophysical Research*, *108*(D18), 8576. https://doi.org/10.1029/2002JD002648

Gao, Y., & Anderson, J. R. (2001). Characteristics of Chinese aerosols determined by individual-particle analysis. *Journal of Geophysical Research*, *106*(D16), 18037–18045. https://doi.org/10.1029/2000JD900725

Ginoux, P. (2003). Effects of nonsphericity on mineral dust modeling. *Journal of Geophysical Research*, *108*(D2), 4052. https://doi.org/10.1029/2002JD002516

Ginoux, P., Chin, M., Tegen, I., Prospero, J. M., Holben, B., Dubovik, O., & Lin, S.-J. (2001). Sources and distributions of dust aerosols simulated with the GOCART model. *Journal of Geophysical Research*, *106*(D17), 20255–20273. https://doi.org/10.1029/2000JD000053

Ginoux, P., Prospero, J. M., Torres, O., & Chin, M. (2004). Long-term simulation of global dust distribution with the GOCART model: Correlation with North Atlantic Oscillation. *Environmental Modelling & Software*, *19*(2), 113–128. https://doi.org/10.1016/S1364-8152(03)00114-2

Hanisch, F., & Crowley, J. N. (2001). The heterogeneous reactivity of gaseous nitric acid on authentic mineral dust samples, and on individual mineral and clay mineral components. *Physical Chemistry Chemical Physics*, *3*(12), 2474–2482. https://doi.org/10.1039/b101700o

Hansen, J. E., & Travis, L. D. (1974). Light scattering in planetary atmospheres. *Space Science Reviews*, *16*(4), 527–610. https://doi.org/10.1007/BF00168069

Heim, E. W., Dibb, J., Scheuer, E., Jost, P. C., Nault, B. A., Jimenez, J. L., et al. (2020). Asian dust observed during KORUS-AQ facilitates the uptake and incorporation of soluble pollutants during transport to South Korea. *Atmospheric Environment*, *224*, 117305. https://doi.org/10.1016/j.atmosenv.2020.117305

Huang, L., Zhao, Y., Li, H., & Chen, Z. (2015). Kinetics of heterogeneous reaction of sulfur dioxide on authentic mineral dust: Effects of relative humidity and hydrogen peroxide. *Environmental Science & Technology*, *49*(18), 10797–10805. https://doi.org/10.1021/acs.est.5b03930

Jacob, D. J. (2000). Heterogeneous chemistry and tropospheric ozone, Atmos. *The Environment Times*, *34*(12–14), 2131–2159. https://doi.org/10.1016/s1352-2310(99)00462-8

Jung, Y., González Abad, G., Nowlan, C. R., Chance, K., Liu, X., Torres, O., & Ahn, C. (2019). Explicit aerosol correction of OMI formaldehyde retrievals. *Earth and Space Science*, *6*(11), 2087–2105. https://doi.org/10.1029/2019EA000702

Kahn, R., West, R., McDonald, D., Rheingans, B., & Mishchenko, M. I. (1997). Sensitivity of multiangle remote sensing observations to aerosol sphericity. *Journal of Geophysical Research*, *102*(D14), 16861–16870. https://doi.org/10.1029/96JD01934

Kahnert, M., & Kylling, A. (2004). Radiance and flux simulations for mineral dust aerosols: Assessing the error due to using spherical or spheroidal model particles. *Journal of Geophysical Research*, *109*(D9), D09203. https://doi.org/10.1029/2003JD004318

Kalashnikova, O. V., Kahn, R., Sokolik, I. N., & Li, W.-H. (2005). Ability of multiangle remote sensing observations to identify and distinguish mineral dust types: Optical models and retrievals of optically thick plumes. *Journal of Geophysical Research*, *110*(D18), D18S14. https://doi.org/10.1029/2004JD004550

Kalashnikova, O. V., & Sokolik, I. N. (2002). Importance of shapes and compositions of wind-blown dust particles for remote sensing at solar wavelengths. *Geophysical Research Letters*, *29*(10), 38-1–38–4. https://doi.org/10.1029/2002GL014947

Kalashnikova, O. V., & Sokolik, I. N. (2004). Modeling the radiative properties of nonspherical soil-derived mineral aerosols. *Journal of Quantitative Spectroscopy and Radiative Transfer*, *87*(2), 137–166. https://doi.org/10.1016/j.jqsrt.2003.12.026

Kim, J., Jeong, U., Ahn, M.-H., Kim, J. H., Park, R. J., Lee, H., et al. (2020). New Era of air quality monitoring from Space: Geostationary Environment Monitoring Spectrometer (GEMS). *Bulletin of the American Meteorological Society*, *101*(1), E1–E22. https://doi.org/10.1175/BAMS-D-18-0013.1

Kok, J. F., Ridley, D. A., Zhou, Q., Miller, R. L., Zhao, C., Heald, C. L., et al. (2017). Smaller desert dust cooling effect estimated from analysis of dust size and abundance. *Nature Geoscience*, *10*(4), 274–278. https://doi.org/10.1038/ngeo2912

Kok, J. F., Ward, D. S., Mahowald, N. M., & Evan, A. T. (2018). Global and regional importance of the direct dust-climate feedback. *Nature Communications*, *9*(1), 241. https://doi.org/10.1038/s41467-017-02620-y

Laaksonen, A., Malila, J., Nenes, A., Hung, H.-M., & Chen, J.-P. (2016). Surface fractal dimension, water adsorption efficiency and cloud nucleation activity of insoluble aerosol. *Scientific Reports*, *6*(1), 25504. https://doi.org/10.1038/srep25504

Levelt, P. F., van den Oord, G. H. J., Dobber, M. R., Malkki, A., Visser, H., De Vries, J., et al. (2006). The ozone monitoring instrument. *IEEE Transactions on Geoscience and Remote Sensing*, *44*(5), 1093–1101. https://doi.org/10.1109/TGRS.2006.872333

Li, C., Kattawar, G. W., & Yang, P. (2004). Effects of surface roughness on light scattering by small particles. *Journal of Quantitative Spectroscopy and Radiative Transfer*, *89*(1), 123–131. https://doi.org/10.1016/j.jqsrt.2004.05.016

Lin, J.-T., Liu, M.-Y., Xin, J.-Y., Boersma, K. F., Spurr, R., Martin, R., & Zhang, Q. (2015). Influence of aerosols and surface reflectance on satellite NO_2 retrieval: Seasonal and spatial characteristics and implications for NO_x emission constraints. *Atmospheric Chemistry and Physics*, *15*(19), 11217–11241. https://doi.org/10.5194/acp-15-11217-2015

Lin, J.-T., Martin, R. V., Boersma, K. F., Sneep, M., Stammes, P., Spurr, R., et al. (2014). Retrieving tropospheric nitrogen dioxide from the Ozone Monitoring Instrument: Effects of aerosols, surface reflectance anisotropy, and vertical profile of nitrogen dioxide. *Atmospheric Chemistry and Physics*, *14*(3), 1441–1461. https://doi.org/10.5194/acp-14-1441-2014

Lin, W., Bi, L., & Dubovik, O. (2018). Assessing superspheroids in modeling the scattering matrices of dust aerosols. *Journal of Geophysical Research: Atmospheres*, *123*(24), 13917–13943. https://doi.org/10.1029/2018JD029464

Liou, K. N. (2002). *An introduction to atmospheric radiation*. Elsevier.

Liu, X., Turner, J. R., Hand, J. L., Schichtel, B. A., & Martin, R. V. (2022). A global-scale mineral dust equation. *Journal of Geophysical Research: Atmospheres*, *127*(18), e2022JD036937. https://doi.org/10.1029/2022JD036937

Liu, Y., Arnott, W. P., & Hallett, J. (1999). Particle size distribution retrieval from multispectral optical depth: Influences of particle nonsphericity and refractive index. *Journal of Geophysical Research*, *104*(D24), 31753–31762. https://doi.org/10.1029/1998JD200122

Majumdar, A., & Bhushan, B. (1990). Role of fractal geometry in roughness characterization and contact mechanics of surfaces. *Journal of Tribology*, *112*(2), 205–216. https://doi.org/10.1115/1.2920243

Marcolli, C. (2014). Deposition nucleation viewed as homogeneous or immersion freezing in pores and cavities. *Atmospheric Chemistry and Physics*, *14*(4), 2071–2104. https://doi.org/10.5194/acp-14-2071-2014

Marcolli, C. (2020). Technical note: Fundamental aspects of ice nucleation via pore condensation and freezing including Laplace pressure and growth into macroscopic ice. *Atmospheric Chemistry and Physics*, *20*(5), 3209–3230. https://doi.org/10.5194/acp-20-3209-2020

Martin, R. V., Jacob, D. J., Yantosca, R. M., Chin, M., & Ginoux, P. (2003). Global and regional decreases in tropospheric oxidants from photochemical effects of aerosols. *Journal of Geophysical Research*, *108*(D3), 4097. https://doi.org/10.1029/2002JD002622

Meng, J., Huang, Y., Leung, D. M., Li, L., Adebiyi, A. A., Ryder, C. L., et al. (2022). Improved parameterization for the size distribution of emitted dust aerosols reduces model underestimation of super coarse dust. *Geophysical Research Letters*, *49*(8), e2021GL097287. https://doi.org/10.1029/2021GL097287

Meng, J., Martin, R. V., Ginoux, P., Hammer, M., Sulprizio, M. P., Ridley, D. A., & van Donkelaar, A. (2021). Grid-independent high-resolution dust emissions (v1.0) for chemical transport models: Application to GEOS-Chem (12.5.0). *Geoscientific Model Development*, *14*(7), 4249–4260. https://doi.org/10.5194/gmd-14-4249-2021

Mishchenko, M. I., Travis, L. D., Kahn, R. A., & West, R. A. (1997). Modeling phase functions for dustlike tropospheric aerosols using a shape mixture of randomly oriented polydisperse spheroids. *Journal of Geophysical Research*, *102*(D14), 16831–16847. https://doi.org/10.1029/96JD02110

Mishchenko, M. I., Travis, L. D., & Lacis, A. A. (2002). *Scattering, absorption, and emission of light by small particles*. Cambridge University Press.

Nakajima, T., Tanaka, M., Yamano, M., Shiobara, M., Arao, K., & Nakanishi, Y. (1989). Aerosol optical characteristics in the yellow sand events observed in May, 1982 at Nagasaki-Part II models. *Journal of the Meteorological Society of Japan. Ser. II*, *67*(2), 279–291. https://doi.org/10.2151/jmsj1965.67.2_279

Okada, K., Heintzenberg, J., Kai, K., & Qin, Y. (2001). Shape of atmospheric mineral particles collected in three Chinese arid-regions. *Geophysical Research Letters*, *28*(16), 3123–3126. https://doi.org/10.1029/2000GL012798

Okada, K., Kobayashi, A., Iwasaka, Y., Naruse, H., Tanaka, T., & Nemoto, O. (1987). Features of individual Asian dust-storm particles collected at Nagoya, Japan. *Journal of the Meteorological Society of Japan*, *65*(3), 515–521. https://doi.org/10.2151/jmsj1965.65.3_515

Palmer, P. I., Jacob, D. J., Chance, K., Martin, R. V., Spurr, R. J. D., Kurosu, T. P., et al. (2001). Air mass factor formulation for spectroscopic measurements from satellites: Application to formaldehyde retrievals from the Global Ozone Monitoring Experiment. *Journal of Geophysical Research*, *106*(D13), 14539–14550. https://doi.org/10.1029/2000JD900772

Pan, X., Uno, I., Wang, Z., Nishizawa, T., Sugimoto, N., Yamamoto, S., et al. (2017). Real-time observational evidence of changing Asian dust morphology with the mixing of heavy anthropogenic pollution. *Scientific Reports*, *7*(1), 1. https://doi.org/10.1038/s41598-017-00444-w

Ramachandran, P. A. (2014). *Advanced transport phenomena: Analysis, modeling, and computations*. Cambridge University Press.

Reid, E. A., Reid, J. S., Meier, M. M., Dunlap, M. R., Cliff, S. S., Broumas, A., et al. (2003). Characterization of African dust transported to Puerto Rico by individual particle and size segregated bulk analysis. *Journal of Geophysical Research*, *108*(D19), 8591. https://doi.org/10.1029/2002JD002935

Rutherford, D. W., Chiou, C. T., & Eberl, D. D. (1997). Effects of exchanged cation on the microporosity of montmorillonite. *Clays and Clay Minerals*, *45*(4), 534–543. https://doi.org/10.1346/CCMN.1997.0450405

Ryder, C. L., Marenco, F., Brooke, J. K., Estelles, V., Cotton, R., Formenti, P., et al. (2018). Coarse-mode mineral dust size distributions, composition and optical properties from AER-D aircraft measurements over the tropical eastern Atlantic. *Atmospheric Chemistry and Physics*, *18*(23), 17225–17257. https://doi.org/10.5194/acp-18-17225-2018

Singh, I. (2024). Effect of dust morphology on aerosol optics in the GEOS-Chem chemical transport model, on UV-Vis trace gas retrievals, and on surface area available for reactive uptake [Dataset]. *Zenodo*. https://doi.org/10.5281/zenodo.10914522

Sinyuk, A., Torres, O., & Dubovik, O. (2003). Combined use of satellite and surface observations to infer the imaginary part of refractive index of Saharan dust. *Geophysical Research Letters*, *30*(2), 1081. https://doi.org/10.1029/2002GL016189

Spurr, R. J. D. (2006). Vlidort: A linearized pseudo-spherical vector discrete ordinate radiative transfer code for forward model and retrieval studies in multilayer multiple scattering media. *Journal of Quantitative Spectroscopy and Radiative Transfer*, *102*(2), 316–342. https://doi.org/10.1016/j.jqsrt.2006.05.005

Tegen, I., & Lacis, A. A. (1996). Modeling of particle size distribution and its influence on the radiative properties of mineral dust aerosol. *Journal of Geophysical Research*, *101*(D14), 19237–19244. https://doi.org/10.1029/95JD03610

van Donkelaar, A., Martin, R. V., & Park, R. J. (2006). Estimating ground-level PM2.5 using aerosol optical depth determined from satellite remote sensing. *Journal of Geophysical Research*, *111*(D21), D21201. https://doi.org/10.1029/2005JD006996

Varga, G., Dagsson-Waldhauserová, P., Gresina, F., & Helgadottir, A. (2021). Saharan dust and giant quartz particle transport towards Iceland. *Scientific Reports*, *11*(1), 11891. https://doi.org/10.1038/s41598-021-91481-z

Veefkind, J. P., Aben, I., McMullan, K., Förster, H., de Vries, J., Otter, G., et al. (2012). TROPOMI on the ESA sentinel-5 precursor: A GMES mission for global observations of the atmospheric composition for climate, air quality and ozone layer applications. *Remote Sensing of Environment*, *120*, 70–83. https://doi.org/10.1016/j.rse.2011.09.027

Wang, J., Liu, X., Christopher, S. A., Reid, J. S., Reid, E., & Maring, H. (2003). The effects of non-sphericity on geostationary satellite retrievals of dust aerosols. *Geophysical Research Letters*, *30*(24), 2293. https://doi.org/10.1029/2003GL018697

Xu, X., & Wang, J. (2019). UNL-VRTM, A testbed for aerosol remote sensing: Model developments and applications. In A. Kokhanovsky (Ed.), *Springer series in light scattering* (pp. 1–69). Springer International Publishing. https://doi.org/10.1007/978-3-030-20587-4_1

Yang, P., Liou, K. N., Mishchenko, M. I., & Gao, B.-C. (2000). Efficient finite-difference time-domain scheme for light scattering by dielectric particles: Application to aerosols. *Applied Optics*, *39*(21), 3727–3737. https://doi.org/10.1364/AO.39.003727

Yang, S., Liang, M., Yu, B., & Zou, M. (2014). Permeability model for fractal porous media with rough surfaces. *Microfluidics and Nanofluidics*, *18*(5–6), 1085–1093. https://doi.org/10.1007/s10404-014-1500-1

Yu, B., & Cheng, P. (2002). Fractal models for the effective thermal conductivity of bidispersed porous media. *Journal of Thermophysics and Heat Transfer*, *16*(1), 22–29. https://doi.org/10.2514/2.6669

Zhai, S., Jacob, D. J., Pendergrass, D. C., Colombi, N. K., Shah, V., Yang, L. H., et al. (2023). Coarse particulate matter air quality in East Asia: Implications for fine particulate nitrate. *Atmospheric Chemistry and Physics*, *23*(7), 4271–4281. https://doi.org/10.5194/acp-23-4271-2023

Zhang, L., Kok, J. F., Henze, D. K., Li, Q., & Zhao, C. (2013). Improving simulations of fine dust surface concentrations over the Western United States by optimizing the particle size distribution. *Geophysical Research Letters*, *40*(12), 3270–3275. https://doi.org/10.1002/grl.50591

Zoogman, P., Liu, X., Suleiman, R. M., Pennington, W. F., Flittner, D. E., Al-Saadi, J. A., et al. (2017). Tropospheric Emissions: Monitoring of pollution (TEMPO). *Journal of Quantitative Spectroscopy and Radiative Transfer*, *186*, 17–39. https://doi.org/10.1016/j.jqsrt.2016.05.008

Zubko, E., Muinonen, K., Shkuratov, Y., Videen, G., & Nousiainen, T. (2007). Scattering of light by roughened Gaussian random particles. *Journal of Quantitative Spectroscopy and Radiative Transfer*, *106*(1–3), 604–615. https://doi.org/10.1016/j.jqsrt.2007.01.050